



Research paper

Structural test and FEM analysis of a thermal bridge connection employing the UHPC system for concrete cladding wall

Nguyen Huu Cuong ^{a,b}, Hyoseo An ^a, Tran-Van Han ^{a,c}, Sanghee An ^d, Jiuk Shin ^e, Kihak Lee ^{a,*}

^a Deep Learning Architecture Research Center, Department of Architectural Engineering, Sejong University, 209 Neungdong-ro, Gwangjin-gu, Seoul 05006, South Korea

^b Department of Civil Engineering, Vinh University, Vinh 461010, Viet Nam

^c Faculty of Civil Engineering, Mien Trung University of Civil Engineering, Tuy Hoa and Danang, Viet Nam

^d JeongYang SG Co., LTD, South Korea

^e Department of Architectural Engineering, Gyeongsang National University, Jinju 52828, South Korea

ARTICLE INFO

Keywords:

Thermal bridge
Experiment
Shear strength
UHPC
LS-DYNA

ABSTRACT

The paper describes the technical design used to develop a structure model that improved thermal insulation properties and structural performance. This study experimentally and analytically investigated the shear capacity of a precast ultra-high performance concrete (UHPC) rib with a concrete cladding wall through the shear keys connection. The structural performance was examined by conducting tests on five specimens under conditions of static loading of the UHPC rib with and without shear keys. The test results revealed that the structural load capacity is significantly affected by changes to the dimensions and design of the shear key, as well as the eccentricity distance in these specimens, the load capacity was approximately 3 to 4 times higher compared to conventional solutions. Numerical models were built to simultaneously predict the shear capacity of structures with varying loading positions and crack failure. These results demonstrated that the proposed modeling may be effectively used to verify the experimental results. Several important input parameters, a constitutive model, and a bar-concrete interface in the LS-DYNA program are suggested.

1. Introduction

Reinforced concrete precast technology is frequently employed in modern buildings. This high-quality and durable technology allows easy installation, making assembly and disassembly simple, while addressing a variety of issues such as shortages of technical staff, an aging workforce, and decreased professionalism. However, ensuring that the structure's connecting section is sufficiently tight can be challenging, impair the total energy efficiency of the insulation, and substantially influence user comfort due to damage and internal deformation [1], [2].

To address the loss of insulation performance caused by the discontinuity of the insulation resistance, Keller et al. [3], Riebel et al. [4], [5], developed a hybrid-GFRP/steel joint for thermal insulation in balcony slab at an insulating layer location of the facade. Cuong et al. [6] investigated a new design that incorporates a shear key connection between the slab and wall to enhance structural performance. In this

study, UHPC was employed in the structure [7], [8], [9], [10], [11], [12], [13]. The insulation is inserted between the ribs to ensure insulation performance and limit energy loss in the building [14], [15], [16]. As shown in Fig. 1, a thermal bridge occurs on the cladding wall of frame system. Cladding walls are exterior building envelope components that are connected and secured using UHPC ribs and stirrups. To prevent heating and cooling energy losses and reduced insulation performance, it is possible to install a frame into which insulation is inserted in the lower part of the cladding wall. The basic components of the connection are the cladding wall, UHPC rib, and reinforcing stirrup bars. These elements are integrated to connect, support, enclose, and protect the building structure.

The novel of this work is a new design that was developed to enhance the overall structural load capacity in residential buildings and designed to facilitate convenient on-site installation after factory production. The UHPC rib is a form of cantilever on a cladding wall and is primarily impacted by shear stress and moment when transferred to

* Corresponding author.

E-mail address: kihaklee@sejong.ac.kr (K. Lee).

Table 1
Mix proportion of UHPC (Unit: kg/m^3).

Materials	Cement	Silica	Sand	Silica powder	Micro silica	Superplasticizer	Steel fiber	Water (l/m^3)
UHPC	830	220	500	280	330	23	75	190

beams or slabs. It is also subjected to the vertical load of the wall. As a result, it is essential to experimentally verify structural performance and establish bearing capacity as well as economic feasibility. This connection can also be used as the foundation for developing detailed cladding walls and UHPC ribs for residential buildings. Five different specimens were built and tested under static loading to calculate the structural performance of the wall joint with other components in the building. Structural features such as crack appearance, fracture patterns, deformability, strength, and stiffness were analyzed.

Recent studies have shown that LS-DYNA is very effective for simulating cracks and failure behaviors in reinforced concrete structures. The MAT072R3 model (KCC), the MAT084/085 model (Winfrith), the MAT159 model (CSC), and the MAT273 model (CDP) are frequently used [17], [18], [19], [20], [21], [22], [23], [24], [25], [26]. The Winfrith model can predict the mechanical behavior of concrete, including the position of cracks. Other concrete models, such as the KCC model, are also available to predict the ultimate load. In this study, the numerical models were carried out using the KCC and Winfrith models simultaneously. Both the KCC and Winfrith models can be used to predict the behavior of concrete with acceptable accuracy. The authors chose to integrate the two models, and these models matched the experimental data well in terms of peak load as well as the cracks in the wall and UHPC rib.

This paper investigated the significance of thermal bridges, particularly the load-bearing mechanism of the structure. The effects of concrete strength, dimensions, and number of shear keys, as well as the location of the load, were examined by experiments and numerical models. These factors played important roles in improving the load capacity of structures. The LS-DYNA generated numerical models, which were used to analyze the load-displacement curves and cracks inside and outside of the concrete. Specifically, a parametric study was conducted to determine the position of damage and predict the load capacity of these structures. Also, some parameters of the KCC, Winfrith models, and the type of contact between the concrete and reinforcement were recommended to accurately simulate the behavior of the materials, which may be applied in future research. The study showed that the mixed model was the suitable model in terms of accuracy and reliability.

The paper includes six sections, as follows: Section 1 shows the purpose and methodology of the experiments. Next, Section 2 shows the material properties and test program. Section 3 presents the experimental results, and Sections 4 and 5 compare the experimental results with the results from the numerical model LS-DYNA. Section 6 investigates the effect of concrete strength on the components of structures. Finally, important conclusions are summarized in Section 7.

2. Experimental program

2.1. Material properties

Portland cement (Class 1 Normal) has a surface area of 0.28 to 0.34 m^2/g and a density of $830 \text{ kg}/m^3$. The specific surface area and density of silica fume are $220 \text{ kg}/m^3$, 15 to $35 \text{ m}^2/g$, and 42.6 GPa, respectively. The steel fiber volume fraction of 1% was used. Fine sand was measured to be $500 \text{ kg}/m^3$. Table 1 shows the specifics of the UHPC mixture proportions acquired from the manufacturer.

Compression tests of the UHPC were conducted following ASTM C109, ASTM C39, and C1856, on at least three cube specimens with dimensions of $100 \text{ mm} \times 100 \text{ mm} \times 100 \text{ mm}$ [27], [28]. In addition, the compressive strength of standard concrete was determined using a

Table 2
Detailed information on test specimens.

No	Specimen	Extrusion shear key (mm)	Eccentricity distance (mm)	Number shear key
1	SK0-EC100	20	100	-
2	SK1-EC125	20	125	1
3	SK1-EC100	20	100	1
4	SK2-EC30	20	30	2
5	RC-EC100	-	100	-

uniaxial compression test on three cylindrical specimens with 150 mm diameters and 300 mm heights. After being poured, all specimens were kept at room temperature for 28 days. The experiment involved two types of specimens, exhibiting variations dependent on the laboratory condition. The Universal Testing Machine (UTM) with a maximum load capacity of 2000 kN was utilized to determine the strength. According to ASTM C39, the prepared concrete sample should be accurately aligned with the loading axis and put on the bottom platen of the compression testing equipment, centered between the platens [29]. Also, two neoprene pads were put between steels and specimens to ensure a uniform load distribution.

In all specimens, the average compressive strength of concrete at 28-days were 36.1 MPa for conventional concrete and 152.5 MPa for the UHPC specimen. The tensile strength of UHPC was 15 MPa. Figs. 2 and 3 show the concrete compressive strength test on concrete and UHPC composites, respectively. For steel bar diameters of 10 mm, and 13 mm, three specimens were randomly chosen for the tensile tests. According to the test findings, the yield strength of the rebar was calculated using the average of three specimens. The average yield strength of rebars D10 and D13 were 384.3 MPa and 432.5 MPa, respectively.

2.2. Description and construction of the specimens

The experiments were conducted in the structural test laboratory in Ansan, Gyeonggi-do. The experimental program used a total of five test specimens. The experiment included a preliminary investigation of the performance of five specimens with the conventional design. The five specimens consisted of one specimen with two shear-key, two specimens with one shear key, and two specimens without shear key. These specimens were prepared considering various positions of load and the number of shear keys. The 5th RC-EC100 specimen was prepared by pouring simultaneously using conventional concrete and without the presence of a UHPC rib, to evaluate the behavior of the concrete.

The construction processes of the test specimens are shown in Fig. 4. Details of the configuration of the UHPC shear-key connection wall are given in Fig. 5. The sizes of the wall and UHPC rib were $1900 \times 900 \times 150 \text{ mm}^3$ (length \times width \times thickness), and $300 \times 250 \times 240 \text{ mm}^3$ (length \times width \times thickness), respectively. UHPC ribs with and without shear keys were prefabricated to obtain the desired strength, then assembled by casting with wall [30]. D13 reinforcement rebars were designed for the UHPC rib and connected the shear key with the cladding wall. Also, D10 reinforcement rebars were placed following the horizontal and vertical cladding wall.

The information on the shear-key specimens is shown in Table 2. The SK0-EC100 specimens had no shear key, while the SK1-EC125, SK1-EC100, and SK2-EC30 specimens had one or two, respectively. All specimens were combined with a cladding wall with an embedded length of 20 mm. Note that, SK means the number of shear keys in the

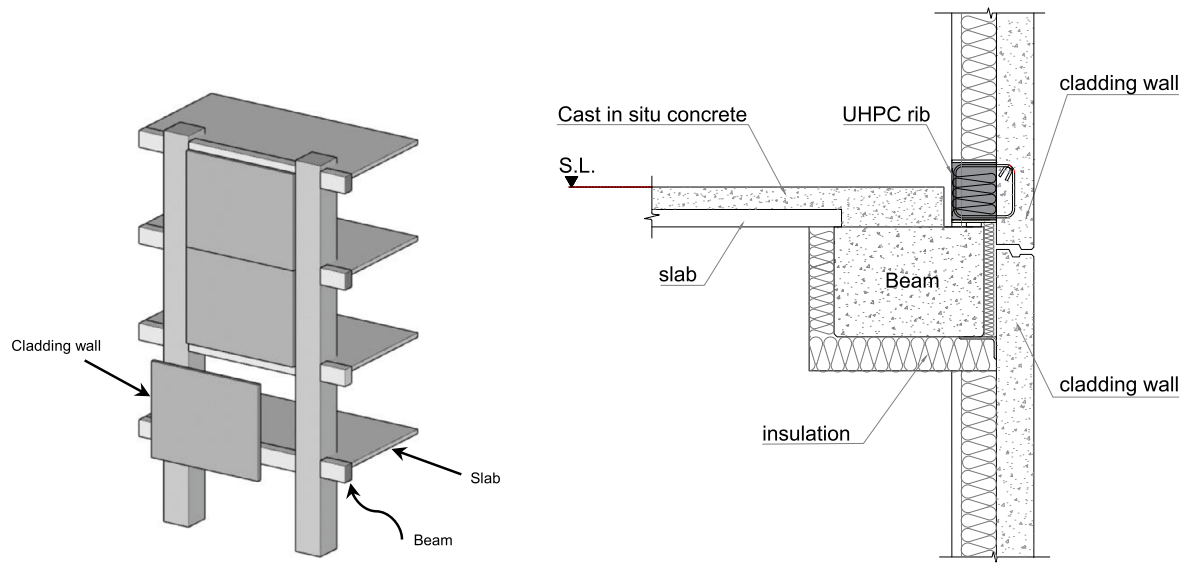


Fig. 1. Section of cladding wall and UHPC rib in the building.

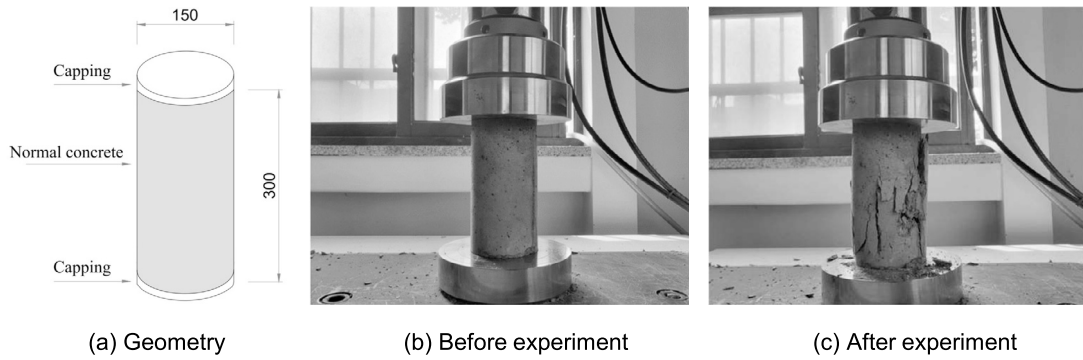


Fig. 2. Compressive strength test on concrete.

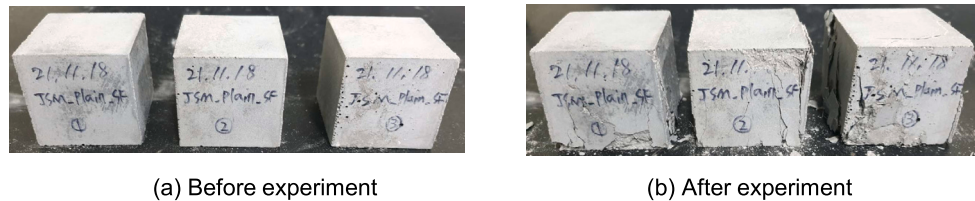


Fig. 3. Compressive strength test on UHPC composites.

rib, and EC is the distance from the point load to the surface of the cladding wall.

2.3. Shear key design

Fig. 5 shows the two types of trapezoidal-shape shear keys including one shear key and two shear keys. The shear key has a depth of 20 mm and an inclined angle of θ , $\tan \theta = 0.25$. In this study, the shape and dimensions of the shear keys were changed to reduce the local stress concentration, also UHPC shear keys can effectively improve shear resistance. Two distinct UHPC shear keys were subjected to testing to assess their respective performances.

2.4. Experiment test setup

The test setup is given in Fig. 6. All specimens were cast using a series of wooden molds, as shown in the figure above. In the experiment,

the UHPC ribs were subjected to horizontal loads using a loading mechanism control. These specimens were subjected to controlled force by a 1000 kN hydraulic UTM universal testing machine. The displacement rate was set to be 3-5 mm/min. During the tests, a load cell was installed horizontally to monitor horizontal load. A steel cylinder (or hinge) was placed on the shear key to ensure that the lateral load was applied to specimens perpendicularly. The load was measured by an internal load cell. A total number of six linear variable differential transducers (LVDT) and four LVDTs were placed on specimens to record the horizontal deformations. One LVDT at the top of the UHPC rib recorded rotation, while another at the outer border of the wall measured slip.

The position of the force applied to the UHPC ribs was varied in order to observe the behavior of the UHPC rib and reinforcing bars, which are affected by changes in shear forces and bending moments. Furthermore, the load capacity of the UHPC ribs was considered to be affected by eccentricity. The experiment was carried out when insulation was added to the upper portion of the wall. Fig. 7 depicts the eccentricities

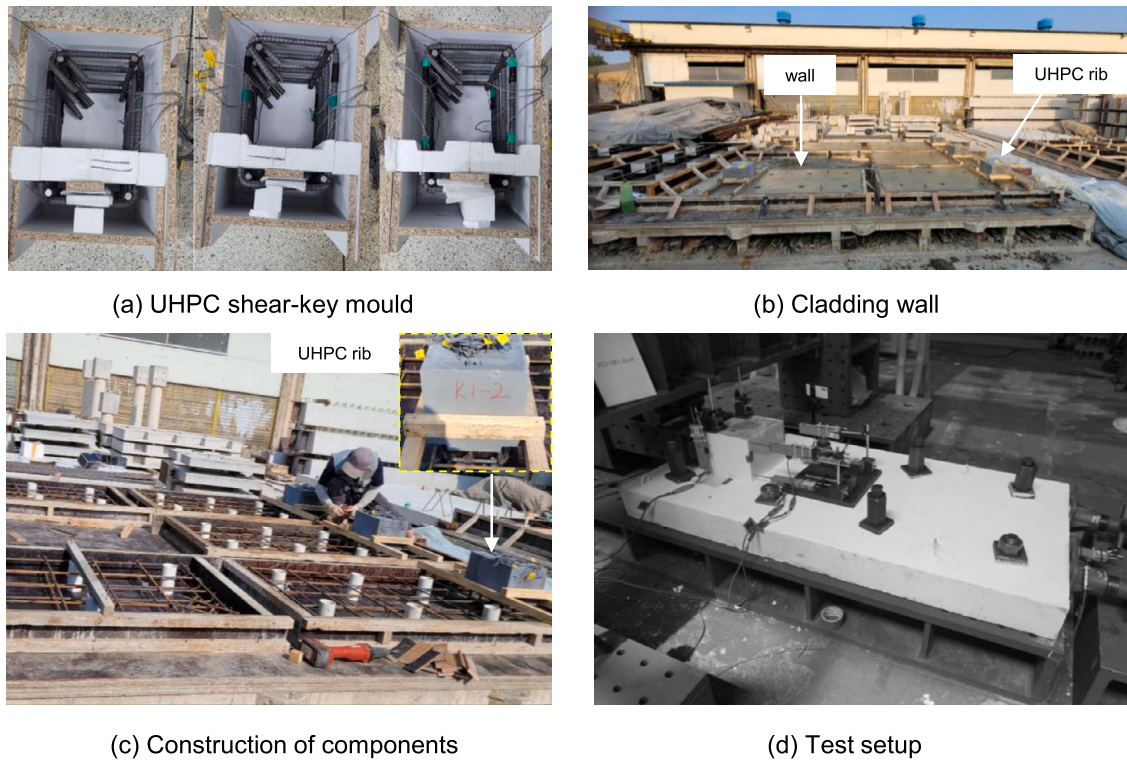


Fig. 4. Construction process of specimens.

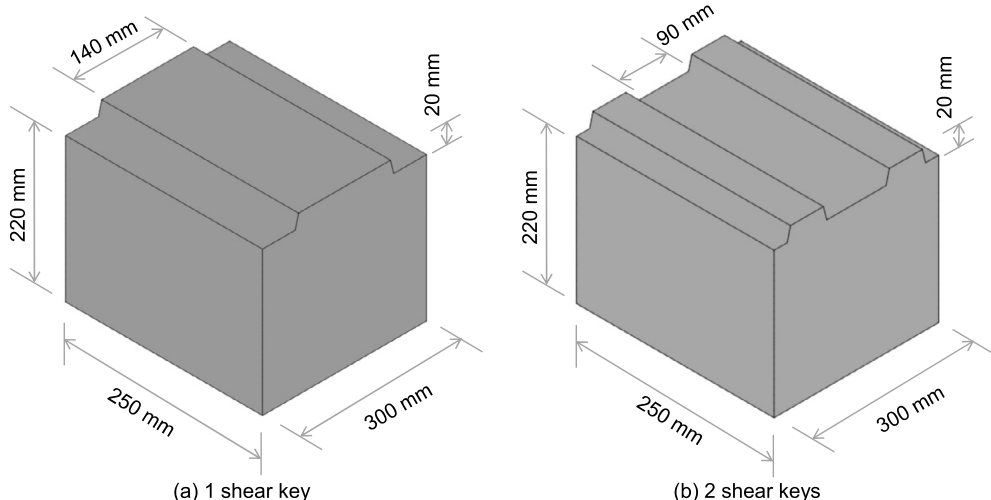


Fig. 5. Design of shear keys.

of 30 mm, 100 mm, and 125 mm used in the actual test. This analysis was conducted to identify a suitable value for eccentricity distance based on structural performance. However, in this work, the test has limitation; the magnitude of the eccentric distance varies within an acceptable range depending on the testing equipment used.

3. Experimental results

3.1. Failure model and crack propagation

In specimens with the UHPC rib, their failure processes and modes were similar. Figs. 8 and 9 depict the cracking patterns of five specimens in the experiment. Two major failure modes were observed for all the test specimens, rib, and wall failure. The failure mode of all specimens occurred in the wall, except for the RC-EC100 case. The failure patterns

in the experiment were influenced by the number of shear keys and the loading position.

For specimen SK0-EC100, the outer shell of the wall was damaged on the left, right, and front side of the rib, as indicated in Fig. 8a. The first crack appeared in the ribs and joints in the load direction. The UHPC rib has a few cracks around the load area, three horizontal rebars that resisted bending can be seen raised, and the concrete cracked and fell off the upper wall surface. An ultimate load in the experiment of about 306.6 kN was obtained at 3.6 mm displacement on the upper part of the rib.

For specimen SK2-EC30, as observed in Fig. 8b, small cracks initially begin to appear in the coating, and the outer wall was damaged on the left and right sides of the ribs. In the lower part of the rib, displacement was 2.7 mm corresponding to an ultimate load of 903.6 kN. As can be

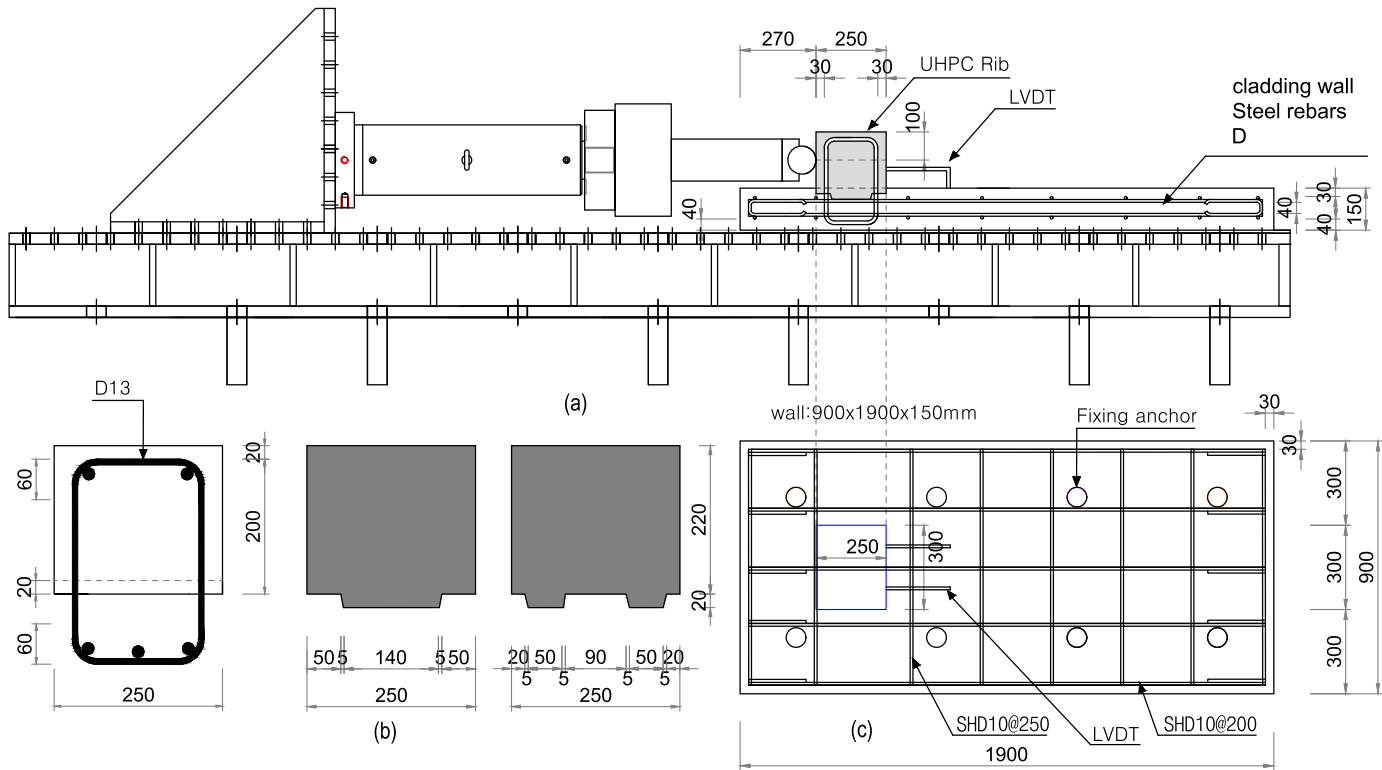


Fig. 6. Details of the test setup: (a) setup plane; (b) shear key; (c) cladding wall.

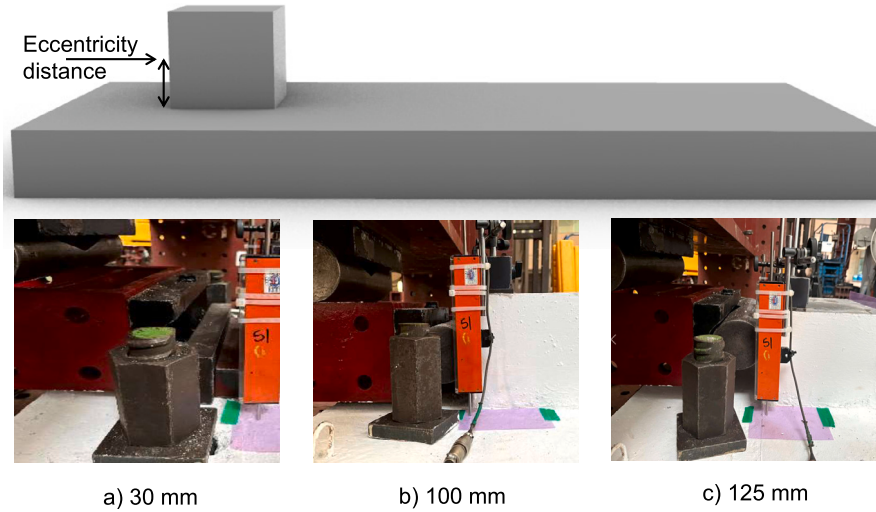


Fig. 7. Loading position.

seen, on the back side of the UHPC rib, the cladding wall concrete has a relatively weak compressive strength and was damaged because of pushing failure.

For specimen SK1-EC125, as the experiment progressed gradually, deformation was only observed in the concrete and the reinforcing bars of the wall. There was a large diagonal crack over the surface of the wall due to lateral loading and crushing near the UHPC rib. In addition, the location of the initial cracking region increased to about 1/2~1/3 of the long wall. When the maximum load was 210.9 kN, a displacement of 1 mm was observed in the lower part of the rib. The failure modes of SK1-EC100 are recorded in Fig. 8c. As observed, a displacement of 1.2 mm occurred in the lower part of the bone side corresponding with a peak load of 320 kN. It seems that increasing the shear keys improved the peak load by about 4.39% (from 306.60 kN to 320.70 kN). When

a bending moment occurred in the ribs, the stirrup bar installed at the end of the UHPC ribs was damaged. Three horizontal rebars were bent and created a visible rise in the concrete.

Unlike the four samples prepared using prefabricated UHPC rib and cast-in-situ wall, the RC-EC100 specimens were produced by in-situ casting of all components. In this case, the compressive strength of the concrete was 36.1 MPa. When load was applied to the RC-rib-wall-EC100 model, the crack in the rib spread and propagated, as indicated in Fig. 8e. Some minor cracks appeared on the top surface of the wall, and the shape of the rib changed as the concrete lower part of the rib was damaged. At the same time, the rib reinforcement was also deformed. At the top of the rib, the peak load was 334.40 kN, while a displacement of 2.5 mm was recorded in the lower part of the rib. This test was different from the rest of the tests. The rib was damaged and

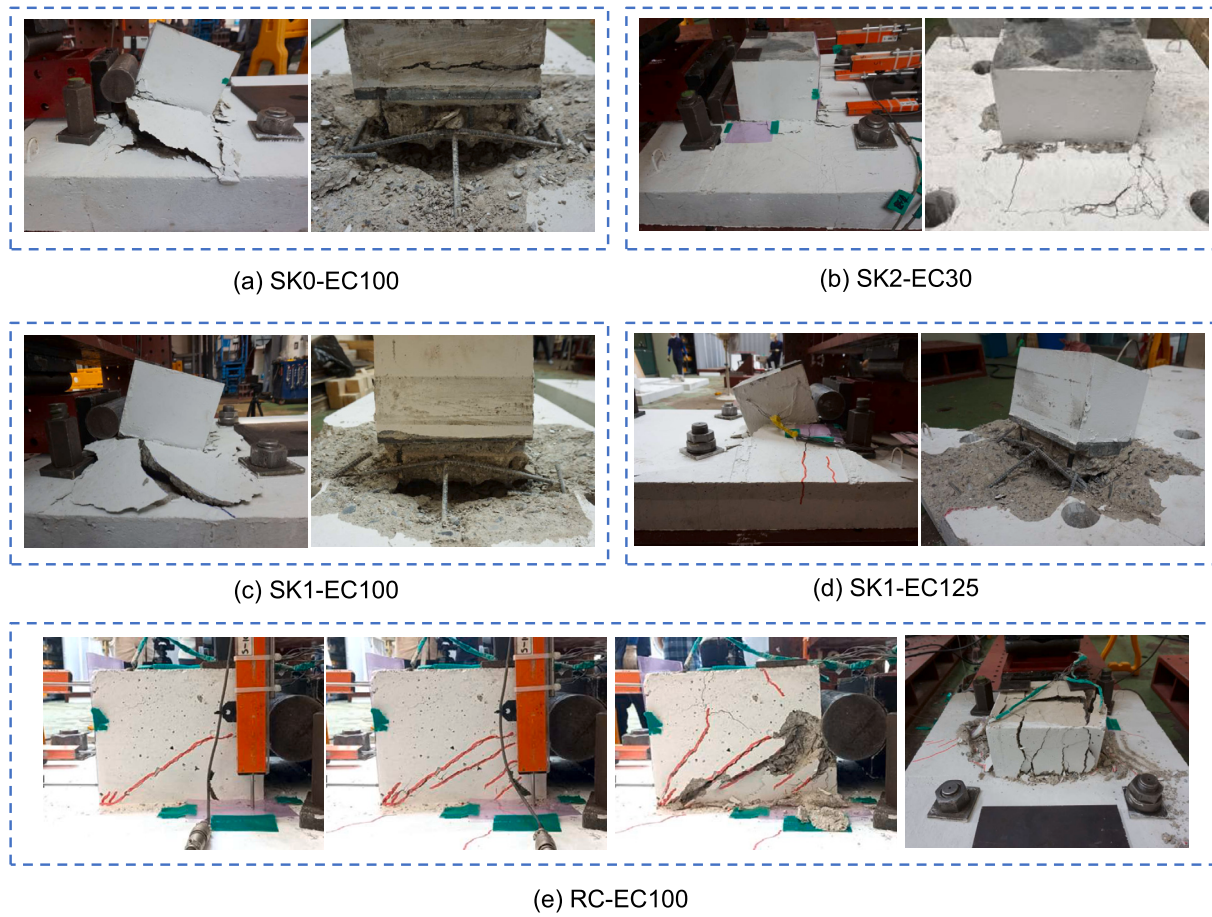


Fig. 8. Damage process and failure mode of specimens.

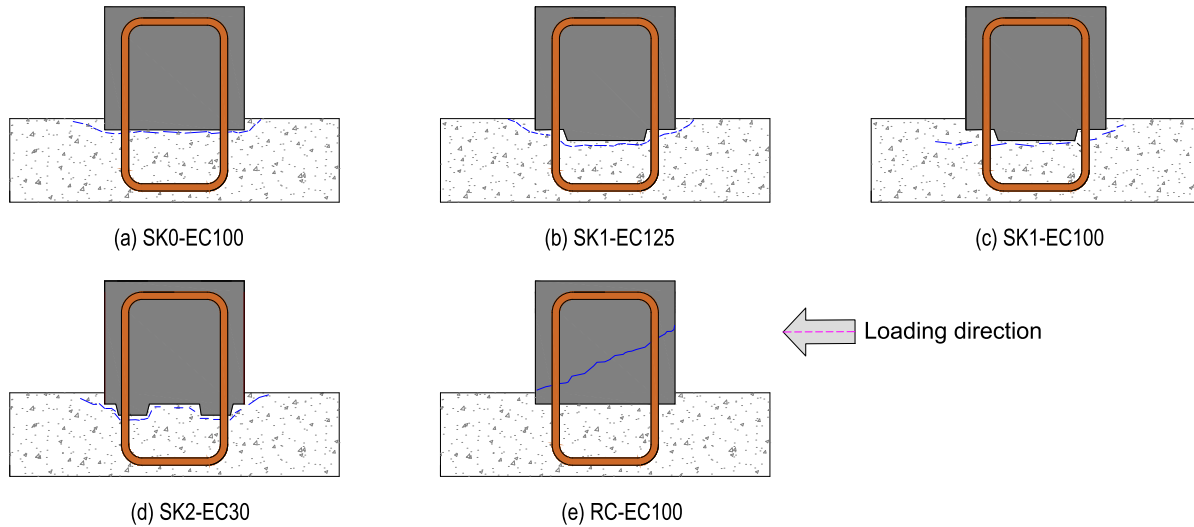


Fig. 9. Crack patterns in reinforced concrete.

deformed, and the deformation was significantly large. Cracks were almost observed on the rib. The reinforcement bars were damaged when the load reached the ultimate load. Then, the initial cracks extended from the center to the left and right corners and slowly expanded. Other diagonal cracks appeared in the wall with a $30^\circ \sim 40^\circ$ angle in the horizontal direction.

In general, similar failure processes and modes were observed across most cases, primarily involving the failure of the UHPC rib and cladding

wall. The main cracks were observed on the top surface of the wall, although RC-EC100 was an exception. For specimens with shear keys, damage primarily occurred in the cladding wall, while for specimens without shear keys, failure modes were similar to those with shear keys, with some cracks appearing in the UHPC rib. There was no change in the shape of the UHPC rib, and most of the deformation occurred only in the concrete and the reinforcing bars of the wall. This is because the high compressive strength of UHPC was 152.5 MPa compared to the

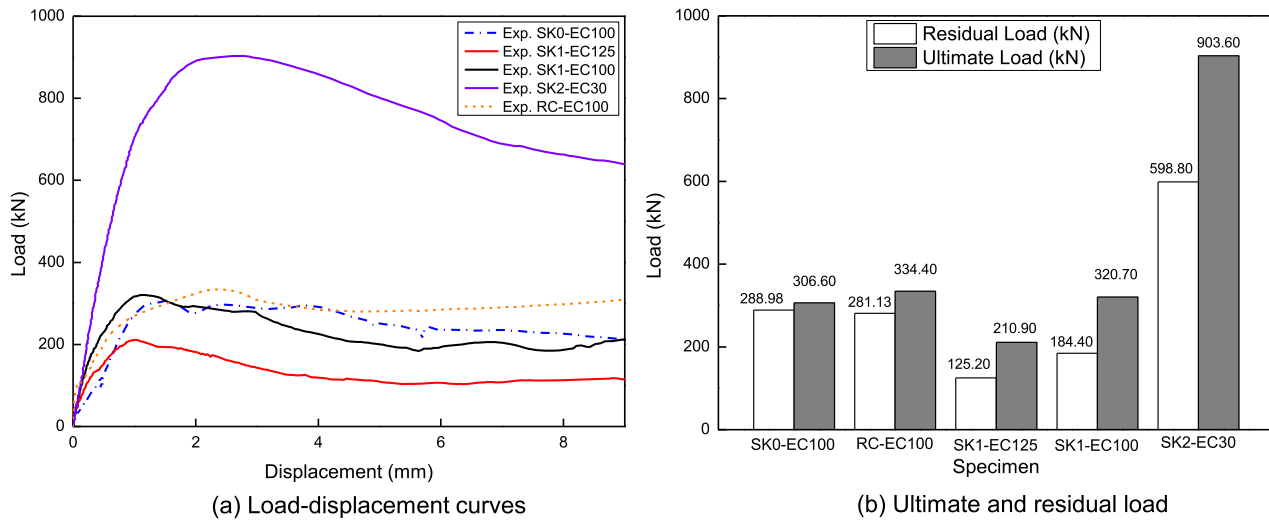


Fig. 10. Results of experiment tests.

wall, with 36.1 MPa. This was attributed to the influence of the superior strength and hardness of UHPC compared to conventional concrete. The presence of shear keys appeared to enhance the structural performance of the specimens, resulting in more controlled failure modes.

3.2. Load-displacement curves

Fig. 10 depicts the average load versus displacement curves for the experiments. During the tests, the load-displacement curves were continuously recorded. The load capacity of the SK2-EC30 (903.60 kN) specimen was the highest of the five cases, meanwhile, the lowest performance was the SK1-EC125 case, with only 210.90 kN. For both cases with an eccentric distance of 100 mm and one shear key, the maximum values of SK1-EC100 and SK0-EC100 were 320.70 kN and 306.6 kN. This value of SK1-EC100 was approximately 4.39% higher than SK0-EC100. These observations suggest that incorporating a shear key, as implemented in the SK1-EC100 specimen, potentially enhances the structural performance and contributes to a more robust load-bearing capacity. For the cast-in-place concrete RC-EC100 specimen, the ultimate load was 334.40 kN, and this value was 8.49% and 4.09% greater than the SK0-EC100 and SK1-EC100, which had values of 306.60 kN and 320.70 kN, respectively. There was little significant difference in the displacement in all cases. The differences were not large, 1.50 mm, 1.01 mm, 1.2 mm, 2.7 mm, and 2.5 mm, respectively, in accordance with Table 6. The initial cracking of specimens appeared at 30.9% to 80.1% of the ultimate load [31].

3.3. Comparison with design formula

In engineering practice, the ACI, AASHTO, JSCE codes, Kaneko et al., as well as Rombach and Specker's formula are the methods commonly used to calculate shear capacity [32], [33], [34], [35], [36], [37], [38]. Except for the ACI code, the rest of the methods separate the shear capacity into two parts, as shown below:

$$V_n = A_{vf} f_y \mu \quad (1)$$

Assumed a crack at an angle of α degrees to the vertical axis,

$$V_n = A_{vf} f_y (\mu \sin \alpha + \cos \alpha) \quad (2)$$

where $\mu = 1.4\lambda$ (concrete placed monolithically); $\lambda = 1$ for normal weight concrete.

AASHTO (1999) established a formula that distinguishes between shear strength supplied by key and the strength conveyed by the smooth surfaces.

Table 3
Summary of shear capacity by design formulation.

No	Specimen	AASHTO	ACI	Rombach Specker	JSCE	K. Yoshio
1	SK0-EC100	-	198.8	-	-	-
2	SK1-EC125	481.5	198.8	754.5	532.0	258.5
3	SK1-EC100	481.5	198.8	754.5	532.0	258.5
4	SK2-EC30	368.9	198.8	560.1	380.0	196.3
5	RC-EC100	-	235.7	-	-	-

$$V_u = A_k \sqrt{f_{ck}} (0.2048\sigma_n + 0.9961) + 0.6A_{sm}\sigma_n \quad (3)$$

where V_u is shear strength; A_k is the area of all keys in the failure plane; f_{ck} is the concrete's compressive strength; σ_n is the compressive stress after allowing for prestress losses.

Rombach and Specker's calculated shear strength equation is

$$V_R = 0.14f'_c A_k + 0.65(A_k + A_{sm})\sigma_n \quad (4)$$

where f'_c and A_{sm} are the concrete's compressive strength and the concrete in contact, respectively; σ_n is normal compressive stress on the concrete.

The formula in JSCE is

$$V_{cw} = \mu f'_{cd} \sigma_{nd}^{1-b} A_{cc} + 0.1A_k f'_c \quad (5)$$

where μ is the average contact friction coefficient; f'_{cd} is the compressive strength (MPa); σ_{nd} average compressive stress acting on the shear plane; A_{cc} is compression zone's shear plane; b is the coefficient that indicates the plane configuration and ranges between 0 and 1.

K. Yoshio et al. [39] established a shear design equation for calculating ultimate shear capacity in concrete shear key joints.

$$V_u = A_k \frac{\ln\left(1 + \frac{f_{ck}}{10}\right)}{100} (49\sigma_n + 233) + 0.6A_{sm}\sigma_n (f_{ck} > 50 \text{ MPa}) \quad (6)$$

where A_k , f_{ck} , σ_n , A_{sm} are the area of the shear keys, characteristic compressive cylinder strength of concrete, and confining pressure at the joint.

Table 3 compares the shear capacities of structures according to AASHTO, ACI, Rombach and Specker, K. Yoshio et al., and JSCE following the equation below. As can be seen, the Rombach and Specker's equation overestimated the shear capacity of the UHPC rib. The value is the highest in all cases. In contrast, the ACI formula underestimated the shear capacity of the structures. Whereas, K. Yoshio et al. appears to be appropriate for SK1 specimen. The difference could be because factors

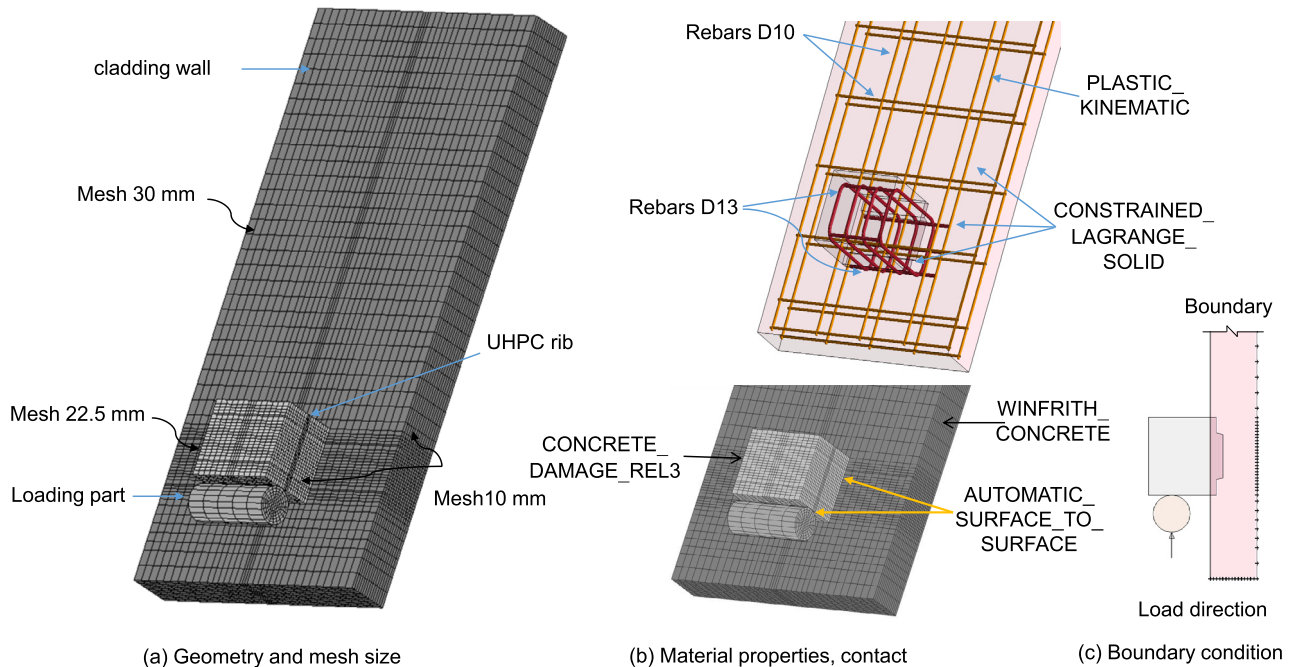


Fig. 11. Details of the numerical model.

such as the shape of the shear keys, and the concrete strength of the wall, are not considered. The contribution of the number of shear keys to the shear strength is not completely taken into account. For one shear key case, the shear strength results from the values of the AASHTO and JSCE methods are higher than the value from the experimental test. The design formulas employed in this section are intended for calculating the shear capacity of contact surfaces. However, applying the existing formula might not accurately predict the shear capacity of structures, even though, according to ACI, the UHPC rib can be treated as a concrete corbel.

4. Numerical analysis

In the LS-DYNA program, simulating the behavior of concrete is extremely complicated because of its non-homogenous and anisotropic nature. These models were carried out using a nonlinear static analysis method. Conventional concrete was modeled using the KCC, and the UHPC was modeled using the Winfrith. While steel reinforcement can be modeled using the *MAT003 [40]. The proposed modeling approach was then validated against the experiment results.

4.1. Geometric model

The complete models are shown in Fig. 11. The UHPC rib and wall were modeled using solid elements, while the steel bars used beam elements. There was a total of 39904 elements (1744 beams, 38160 solids) for SK2-EC30; the rest of the cases were 41689 elements (1744 beams, 39945 solids). The mesh sizes depended on the dimensions of the specimens. In the FE modeling of all specimens, the beam element was used for the steel bar D13. The steel bar was meshed at a 25 mm size, and the cladding wall and UHPC rib were meshed at 10 mm, 22.5 mm, and 30 mm (see Fig. 11a). In all cases, the computational time of the model was suitable for these mesh sizes. These results are found in many previous works [41], [42].

4.2. Constitutive materials models

4.2.1. The KCC model

The KCC model, which is extensively used in research and practical calculation, was used to represent the mechanical behavior of the concrete [43], [44]. Fig. 11 shows a material constitutive relationship from this model, a three-surface damage model form of the plasticity model. It consists of three shear surfaces, the residual failure, initial yield, and maximum yield surfaces. Based on the magnitude of damage determined at the material point, the actual yield surface utilized by the KCC model is interpolated between two of these fixed surfaces. Nine cards are required to define the complete set of model parameters. A complete set of parameters for concrete with a compressive strength of 45.4 MPa was proposed by Youcai Wu et al. [46]. In addition, to predict the behavior of another concrete, varying range 60 to 120 MPa, calibration of the is essential. The scaling factor ϕ is depicted as follows:

$$\phi = \frac{f_c'^n}{f_c'^o} \quad (7)$$

where $f_c'^n$ denotes the concrete's unconfined compressive strength and $f_c'^o = 45.4$ MPa. (See Fig. 12.)

The behavior of the concrete is affected by the parameters material, maximum yield surface (a_0, a_1, a_2), initial yield strength (a_{0y}, a_{1y}, a_{2y}), and residual failure surface (a_0, a_1, a_2). The three pressure-sensitive, independent strength surfaces were calculated

$$\delta_i^n(p) = a_{0i}^n + \frac{p}{a_{1i}^n + a_{2i}^n p} \quad (8)$$

where $a_{0i}^n = \phi a_{0i}^o$; $a_{1i}^n = \phi a_{1i}^o$; $a_{2i}^n = \phi a_{2i}^o$

Accordingly, the input parameters for concrete are given in Table 4. The pressure-volume strain response also involves the use of an Equation-of-State (EOS). The internal energy in the tabular equation of state model may be estimated.

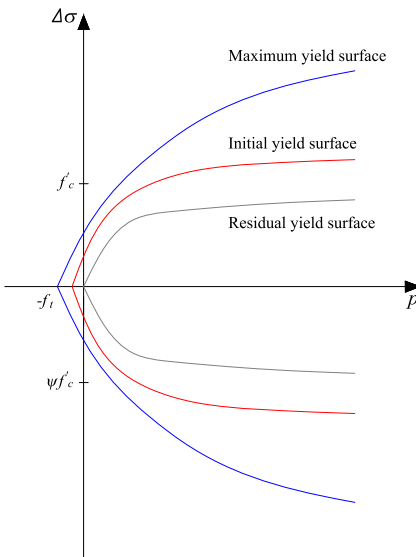
$$P = C(\epsilon_V) + \gamma T(\epsilon_V) E \quad (9)$$

where ϵ_V : volumetric strain; C, T : tabulated points for function; T, γ : unitless. Note that LS-DYNA will extrapolate to determine the pres-

Table 4

Input parameters of the KCC model using the UHPC rib and normal concrete (Unit: MPa).

Parameters	$f'_c = 36.1$	$f'_c = 60$	$f'_c = 90$	$f'_c = 120$	$f'_c = 152.5$	$f'_c = 180$	$f'_c = 200$
a_0	10.64	17.74	26.6	35.47	45.080002	53.209999	59.119999
a_1	0.446300	0.4463	0.4463	0.4463	0.4463	0.4463	0.4463
a_2	0.0022450	0.001347	8.98E-04	6.73E-04	5.30E-04	4.49E-04	4.04E-04
a_{0y}	8.0369997	13.4	20.09	26.790001	34.049999	40.189999	44.650002
a_{1y}	0.625000	0.625	0.625	0.625	0.625	0.625	0.625
a_{2y}	0.0071520	0.004291	0.002861	0.002146	0.001688	0.00143	0.001287
a_{1y}	0.446300	0.4463	0.4463	0.4463	0.4463	0.4463	0.4463
a_{2y}	0.0022450	0.001347	8.98E-04	6.73E-04	5.30E-04	4.49E-04	4.04E-04

**Fig. 12.** The three surfaces of the KCC model [45].

sure. These material parameters were defined using the *EOS_TABULATED_COMPACTION.

4.2.2. The winfrith concrete model

This model, which is a smeared crack model provided in an 8-node single integration point continuum element, was utilized to simulate the concrete behavior. This model provides unconstrained compression and tensile strengths with the aim of creating output data, providing output that includes information about the position and dimensions of the cracks. Furthermore, this model may produce input parameters from a single input value, indicating the concrete's compressive strength. With the input of particular parameters, it enables the automated production of all parameters.

One of the most important capabilities is the ability to provide information on crack propagation in concrete. Note that, the input parameter for tensile cracking must be given. When strain rate effects are disabled, this option determines the crack width, with normal tensile stress equal to 0. Winfrith's crack width formula depends on crack opening displacement. As the displacement of the fracture grows, the crack length expands, propagates, which leads to the creation of a new crack surface. The specific fracture energy is the energy expended per unit area during the cracking process, as depicted in Fig. 13. The crack width w is represented by a constant c

$$c = w \frac{f_t}{G_f} \quad (10)$$

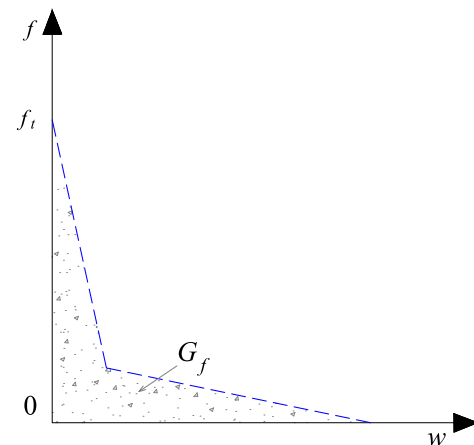
where G_f : specific fracture energy, f_t : tensile strength.

These parameters can be utilized to determine crack width and were calculated utilizing the equation in the CEBFIP Mode [47]. Table 5 lists these input parameters in this model.

Table 5

The parameters associated with the Winfrith concrete material model.

Parameter of concrete	Compressive strength (MPa)				
	25	35	40	45	50
Density (g/mm^3)	0.0023	0.0023	0.0023	0.0023	0.0023
Tensile strength f_t (MPa)	2.75	3.253	3.478	3.689	3.889
Crack width FE (mm)	0.1	0.1	0.1	0.1	0.1
Aggregate size (mm)	16	16	16	16	16

**Fig. 13.** Crack strain softening response in Winfrith model [48].**Table 6**

Input parameters of the *MAT003 model.

Material	Poisson's ratio ν	Density ρ (kg/m^3)	Young's modulus E (GPa)	Yield strength f_y (MPa)
D13	0.265	7830	206	432.5
D10	0.265	7830	206	384.3

4.2.3. Steel model

The Hughes-Liu beam element with 4 integration points was used to represent the reinforcement, which can be modeled using *MAT003. This model can simulate isotropic and kinematic hardening plasticity. Fig. 14 illustrates the elastic and plastic behaviors. Note that E_{tan} is the hardening stiffness of the bilinear stress-strain curve, and β is the hardening parameter ranging between 0 and 1. Table 6 presents the input parameters for the Winfrith model including Poisson's ratio, density, Young's modulus, and yield strength for all of the simulations.

4.3. Rigid material

In these simulations, the loading part of the UHPC rib was modeled as rigid, using *MAT020 [50]. This material offers an effective approach to convert solid elements into a rigid body. Lateral loads were applied to the loading part using the keyword *LOAD_NODE_SET (see Fig. 11c), which were attached to the joints of the UHPC rib. The material properties of the loading part are given in Table 7.

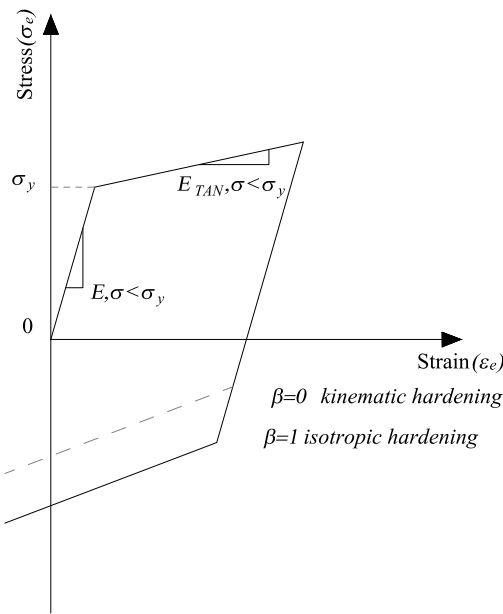


Fig. 14. Stress-strain curve of rebar in the numerical simulation [49].

Table 7
Input parameter of the *MAT020 model.

Variable	ρ	ρ (kg/m^3)	E (GPa)	N	COUPLE	M	ALIAS
Loading part	0.265	7830	206	0	0	0	Blank none

4.4. Contact and boundary conditions

The steel rebar was modeled using the *CONSTRAINED_LAGRANGE_IN_SOLID function. To effectively anticipate the reaction of structures under load, bond-slip behavior modeling in LS-DYNA is critical. It can also be used to analyze the impacts of various types of bonding and optimize designs for better performance and safety. It was assumed that the concrete and steel bars had a perfect connection [51]. This can lead to an overestimation or underestimation of the load capacity of the structures. However, in this study, the structure was subject to static loads, which also reduces calculation time. Therefore, a perfect bond between the rebars and concrete was applied.

The contact option between the UHPC rib and wall was modeled using the *CONTACT_AUTOMATIC_SURFACE_TO_SURFACE function (see Fig. 11b). In all cases, the part of the model was defined as slave or master. These contacts were checked for penetration on either side of the element. The horizontal force was applied to the UHPC rib using a solid rigid cylinder or plate. Deformation of the cylinder and plate were prevented by properly assigning a rigid material to their loading. The movements were constrained following translation in the Z axis and rotation around the X and Y axes.

5. Verification of the FE model

5.1. Ultimate load-displacement curves

Fig. 15 depicts the values and load-displacement curves obtained from the numerical model. To verify the correctness of the developed FEM, they were compared with the experimental results from the five specimens. As can be seen, the model captured the load-displacement behavior of the rib with a maximum strength difference of 5.85%. The shapes of the predicted load-displacement curves were similar to the measured response.

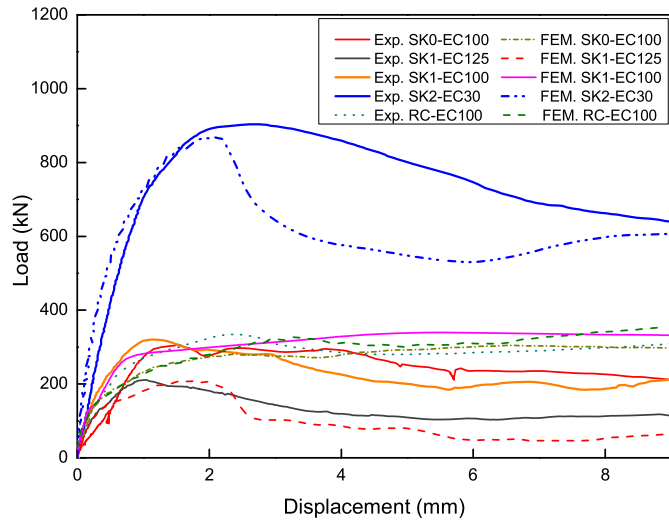


Fig. 15. Load-displacement curves from the experiment and FEM.

As shown in Figs. 16 and 17, for all specimens (SK0-EC100, SK1-EC125, SK1-EC100, SK2-EC30, and RC-EC100), the peak load from the numerical model showed little difference from the experiment. Peak loads in the numerical model of about 304.14 kN, 211.21 kN, 339.45 kN, 876.72 kN, and 325.63 kN were obtained at around 6.65 mm, 1.72 mm, 5.21 mm, 2.03 mm, and 3.37 mm, respectively. It was clear that the highest peak load value was observed at 876.72 kN for SK2-EC30. On the other hand, the lowest value was 211.21 kN for SK1-EC125. This value is about 4 times lower than that of SK2-EC30.

The model predicted load against displacement curve with a maximum strength difference of 0.8%, 0.15%, 5.85%, 2.97%, and 2.69% for five cases. Based on observations from the simulations, the first cracking loads of the SK0-EC100, SK1-EC125, SK1-EC100, and SK2-EC30 models were 206.46 kN, 148.10 kN, 120.34 kN, and 659.39 kN, respectively. SK1-EC100 had the smallest cracking load of 120.34 kN, while SK2-EC30 had the highest cracking load of 659.39 KN. The initial cracking load for the model ranged between 120.34 kN and 659.39 kN. The SK2-EC30 value was about 81.75% higher than the SK1-EC100 value.

In most cases, the load increased almost linearly with displacement to about 80.1% of the ultimate load, after reaching maximum load, and then the load began to decline gradually. It is noted that the elastic stiffness of load-displacement in the numerical model was similar to the experiment. In other words, the values predicted and measured for ultimate load and initial stiffness, were fairly identical.

As can be seen, for the softening phase, the shapes were almost similar for the simulation and experiment. However, the hardening phases were less accurate than the experimental data. This can be explained since these models were created by ignoring many parameters in the numerical model, such as the bond-slip behavior between the concrete and rebar, and there was no investigation of the hourglass effect. Nonetheless, these results are generally acceptable. The findings showed the models were able to predict the load against displacement relationship with sufficient accuracy. The experimental and numerical results of the five specimens are given in Table 8. It presents the peak load and displacement values derived from the five considered specimens as well as the differences between the experimental and numerical results. The experiment results were reliably predicted through the simulation.

This study focuses on predicting the peak strength of structures rather than their post-peak behavior. The anticipation of the maximum force was performed prior to conducting the experimental analysis, and the outcomes exhibited a resemblance to the experimental results, thereby substantiating the precision of both the utilized parameters and the employed model. Consequently, this outcome has a substantial impact on diminishing research expenses by reducing the requisite sample sizes, component optimization, and reducing the duration of testing.

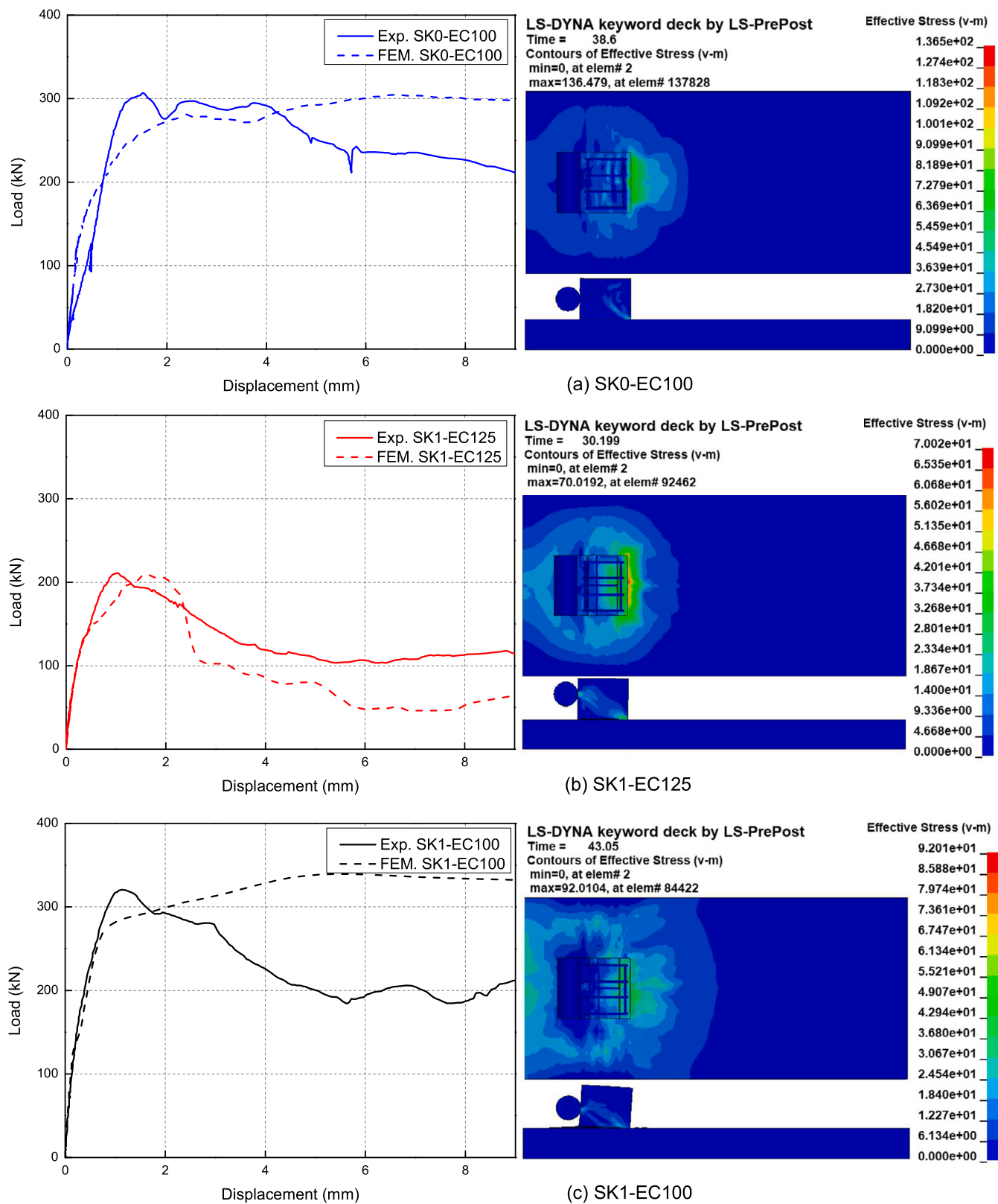


Fig. 16. Comparison of experimental and numerical results: (a) SK0-EC100, (b) SK1-EC125, (c) SK1-EC100.

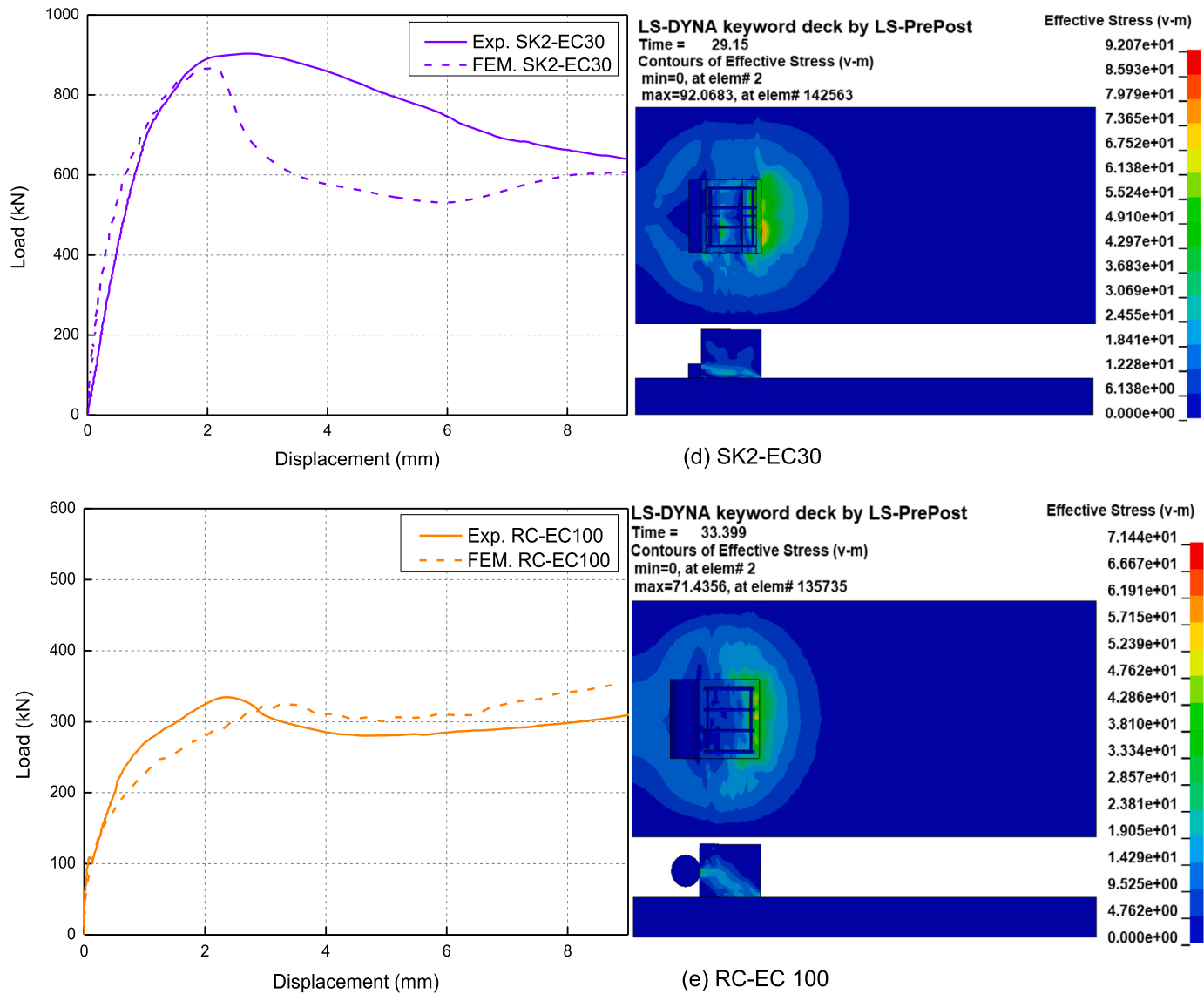


Fig. 17. Comparison of the experimental and numerical results: (d) SK2-EC30, (e) RC-EC 100.

Table 8
Results were obtained from both numerical and experimental methods.

Specimens		SK0-EC100	SK1-EC125	SK1-EC100	SK2-EC30	RC-EC100
Displ. (mm)	Experiment	1.50	1.01	1.20	2.70	2.50
	Numerical	6.65	1.72	5.21	2.03	3.37
Load (kN)	Experiment	306.60	210.90	320.70	903.60	334.40
	Numerical	304.14	211.21	339.45	876.72	325.63
	Error (%)	0.80	0.15	5.85	2.97	2.69

5.2. Failure behavior

The fracture patterns in the numerical models are depicted in Fig. 18. In the FEM simulation, the crack pattern was visible on the top surface of the wall. As observed in the simulation, the majority of damage occurred around the intersection of the wall and the UHPC rib, then the crack expanded to the left and right of the wall. One of the advantages of the FEA is that the crack pattern can be viewed inside the specimen, which cannot be seen from the outside by eyes during the test. Both the KCC model for the UHPC rib and the Winfrith model for the wall predicted the concrete's behavior with acceptable accuracy.

For SK0-EC100, SK1-EC125, SK1-EC100, and SK2-EC30, the failure mechanism was observed as follows: most of the damage occurred around the connection between the UHPC and wall, and cracks in the top face of the cladding wall also began to appear at this time. These cracks then expanded and propagated. Around the concrete cladding wall about 1/3 of the length was slowly damaged by cracks. The UHPC kept its original shape. The region crack was similar, with the final crack pattern can be seen clearly. The main cracks were observed on the edge of the model.

These results demonstrated that the developed models could accurately predict the test results. In this case, the crack length was close to

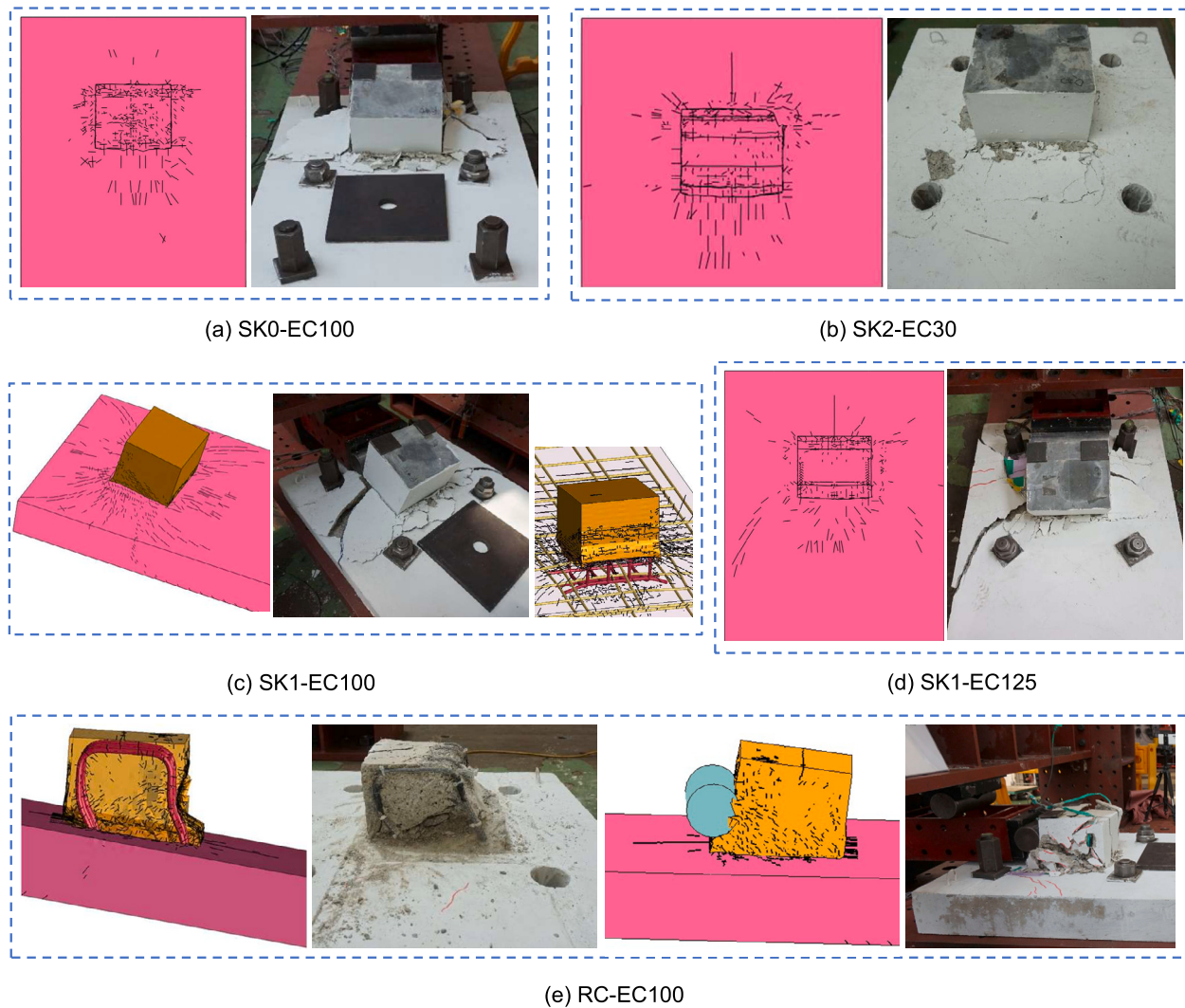


Fig. 18. Comparison of failure pattern between FE and experiment results.

the experimental value. Also, the model could reliably detect the position of the wall concrete failure, as well as recognize the location of the damage, but it was not totally correct for the UHPC concrete failure. The cracking and crushing of the steel bar could be observed.

For the RC-EC100 model, after the first cracking occurred in the rib, the development of micro-cracks occurred between the existing cracks, and the majority of the cracks continued to spread from a position in the middle to the corner of the rib. The rib was deformed at the left, right, and bottom of the rib. Major cracks occurred and were observed on the rib. Then, the rib was severely broken, and could not bear the load anymore. The simulation showed that some minor cracks occurred on the top surface of the wall. Also, as can be seen, the reinforcement bar was damaged. The reinforcing bars embedded in the concrete rib were bent. Fig. 18 shows that the simulation and experiment failure results were similar.

It is noted that the numerical model validation approaches were not standardized. The differences between the numerical model and the experiment result can be explained by some factors. The softening process of the material in the constitutive model was a little different than the actual observed behavior. Therefore, the constitutive model for UHPC needs research and modification, including the hourglass, and bond-slip phenomena in the future.

6. Parametric analysis

In this study, SK1-EC100 and SK2-EC30 were employed to conduct parametric studies of structural performance. The investigation concentrated mainly on the effect of concrete strength on the ultimate load capacity of the models. The designed parameter considered in this study was the strength of the concrete of the UHPC rib and wall. The range of parameters was established as follows: unconfined concrete compressive strength (f'_c) of UHPC rib $f'_{c(UHPC)} = 60 \sim 200$ MPa; wall $f'_{c(wall)} = 25 \sim 50$ MPa. A total number of 20 scenarios were conducted, and the dimensions and material properties of the specimens were constant. In addition, three scenarios with varied eccentricity distances were investigated. The hardening parameter β was varied by 0.1 to 0.9 in the *MAT003 model

6.1. Effect of the concrete strength of the UHPC rib

To examine the influence of concrete compressive strength on the structures, these FE models were carried out using values varying from 60 MPa to 200 MPa. The concrete strength of the wall, yield strength of rebars, and other parameters were unchanged. As depicted in Fig. 19a, the value of the peak load for SK1-EC125 was recorded with 200 MPa at 218.54 kN, while the lowest performance was 155.64 kN at 60 MPa. This value was enhanced by 28.78%. When the compressive strength of

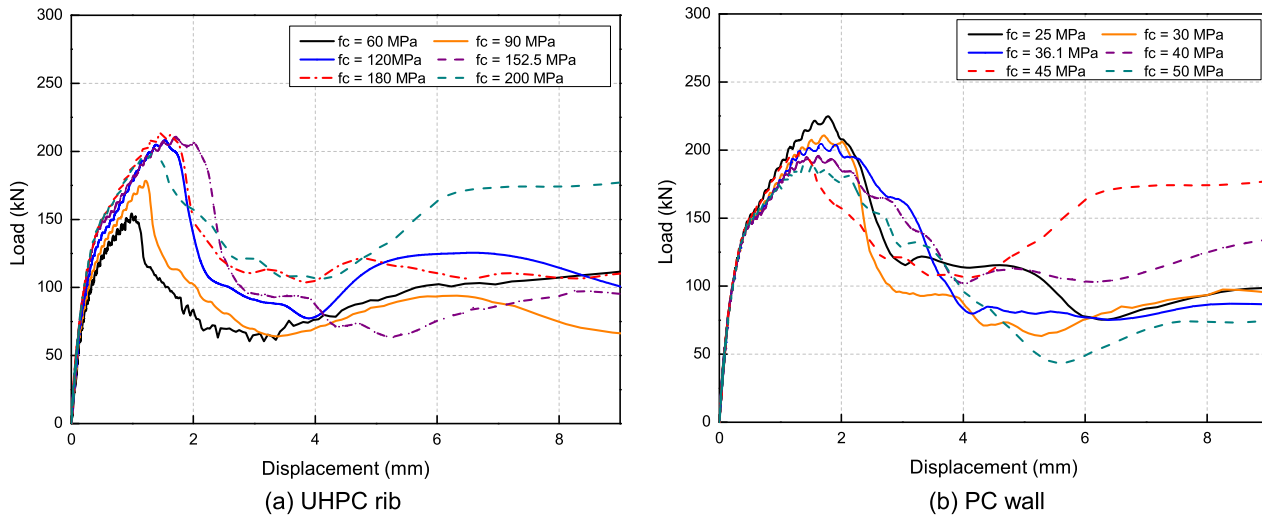


Fig. 19. Results of parametric studies on the SK1-EC125 case.

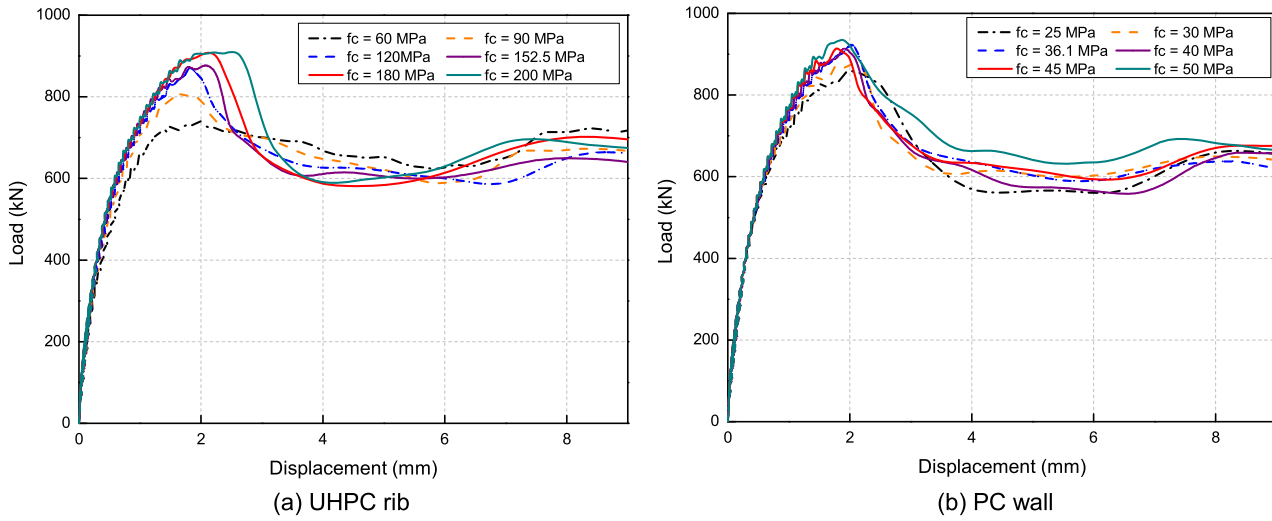


Fig. 20. Results of parametric studies on the SK2-EC30 case.

the concrete increased from 60 MPa to 200 MPa, the rest of the peak loads were 178.52 kN, 208.03 kN, and 213.05 kN, respectively. The simulation results for SK2-EC30 are illustrated in Fig. 20a. The peak loads were 743.94 kN, 813.56 kN, 870.11 kN, 907.87 kN, and 910.23 kN, respectively. Generally, the peak load increased in all cases in both models. Correspondingly, the displacements were 1.97 mm, 1.61 mm, 1.84 mm, 2.18 mm, and 2.51 mm, respectively. The shapes of the load-displacement curves in most cases were similar. As expected, the peak load was strongly influenced by the compressive strength of the concrete.

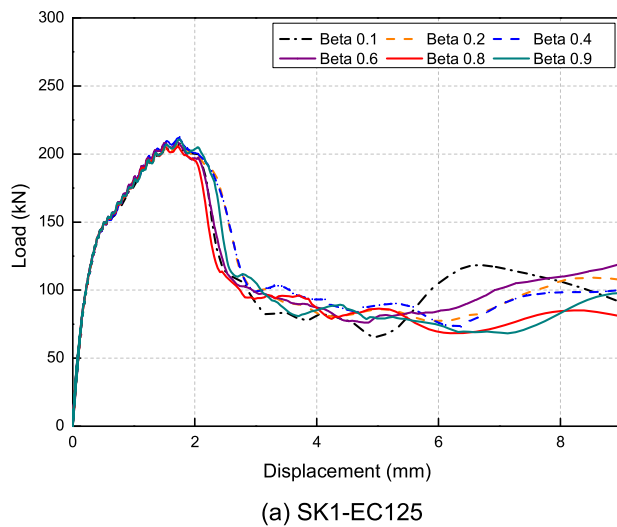
6.2. Effect of concrete strength on cladding wall

The load-displacement curves with various concrete compressive strengths of cladding wall are displayed in Fig. 19b and Fig. 20b. As observed, the lowest values were 190.06 kN, 743.94 kN, while the highest values were 225.85 kN, 934.94 kN for the SK1-EC125 and SK2-EC30 models, respectively. By changing the concrete strength, the peak loads of the models were raised from 12.99% to 15.84%, and conversely. At the same time, the displacements were recorded with corresponding values. The difference is not large with the acceptance rate. Because the concrete modeling was accurate, the shape of the predicted load-

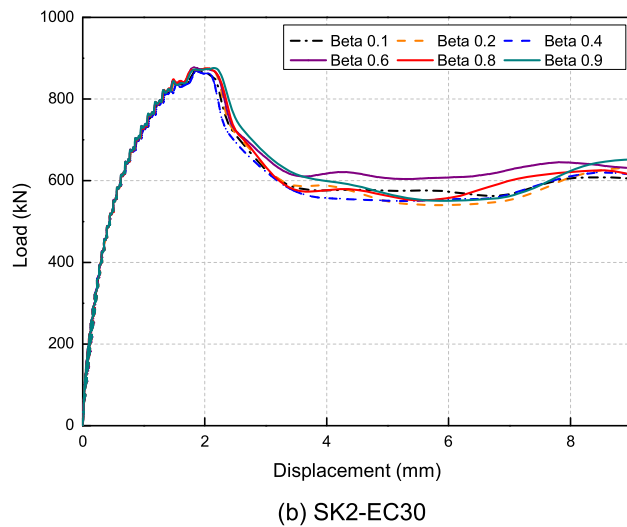
displacement curve is similar to the measured response. This indicates that the concrete compressive strength of the cladding wall, 36.1 MPa, is suitable for both economical and technical benefits.

6.3. Effect of hardening parameter on reinforcement

A total number of 12 scenarios were conducted for SK1-EC125 and SK2-EC30 to investigate the effect of the hardening model. The hardening parameter β is investigated with a value ranging from 0.1 to 0.9. Note that in *MAT003 model, the value of β was greater than 0 and smaller than 1. As shown in Fig. 21, the difference in ultimate load between the β values was less than 0.2% for both models. Therefore, the simulation results are not sensitive to β . Based on the ultimate load and shape of the simulations, these values were compared to experimental results, and the hardening parameter β equal 0.2 was recommended. All results of the parametric study are presented in Appendix A. The effects of the concrete strength and hardening parameter on the ultimate load are summarized in Fig. 23. As expected, the ultimate load increased as concrete strength increased, while the hardening parameter had little effect on the ultimate load.



(a) SK1-EC125



(b) SK2-EC30

Fig. 21. Effect of hardening parameter.

6.4. Predicted crack and failure pattern

The concrete cracks in the 20 models were recorded on the top surface of the cladding wall. The concrete failure behaviors were observed by the LS-DYNA, as shown in Appendix B. The numerical simulation also captured cracks which could not be observed by eye. In all cases, the numerical analyses showed that cracking occurred at the intersection between the rib and the wall. In general, the SK2-EC30 models showed more cracks than the SK1-EC125 models. The types of cracks in the SK1-EC125 models were similar even though the concrete strength changed. As the peak loads increased, these cracks became larger and extended toward the end of the wall. In addition, as observed, most of the cracking occurred at the first and around the end position of the rectangular.

Similarly, these phenomena were observed in the SK2-EC30 models. Because the model had two shear-keys, cracks occurred in three positions, the beginning, middle, and end of the rectangular region. There was a small difference, in that the analytical results showed cracks extending toward two side surfaces of the wall. Based on these results, it was determined that the models were not much of a crack, almost the crack type was minor crack and discontinuum. Some minor cracks did develop toward the side surface of the wall.

A number of crucial recommendations are shown in Table 9, which provides recommendations for the constitutive model as well as its input parameters.

6.5. The effect of eccentricity distance

In this section, the effect of eccentricity distances on the overall structural performance of SK2 specimens is examined. It is noteworthy that, throughout the analysis, concrete strength, yield strength of reinforcement, and loading direction remain constant. Two scenarios of the SK2 model were taken into consideration, involving different eccentricity distances, namely 100 mm and 125 mm. Additionally, one scenario of the SK1 model with eccentricity distances of 30 mm was investigated.

Fig. 22 illustrates that the ultimate loads of SK2-EC125 and SK2-EC100 are 754 kN and 808 kN, respectively. Simultaneously, the displacements are 4.5 mm and 2.61 mm, respectively. The maximum loads in both cases are 13.9% and 7.4%, respectively, lower compared to the SK2-EC30 model (876.72 kN). The ultimate load of the SK1-EC30 is 408.3 kN, exceeding the load of the SK1-EC125, and SK1-EC100 at 211.21 kN, and 339.45 kN, respectively. There is a substantial difference in the ultimate load. Concurrently, the corresponding displacement is 4.7 mm. The ultimate load of the model is significantly enhanced by changing eccentricity distances, with ultimate loads 93.3%,

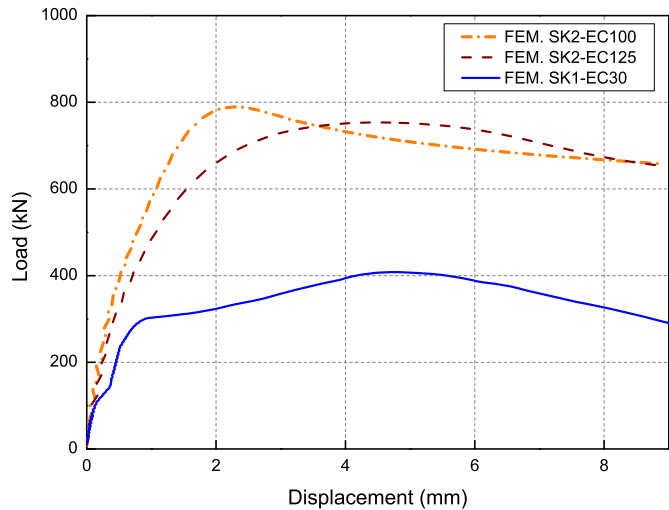


Fig. 22. Effect of eccentricity distances on the structural performance.

20.3% higher than the two models. This value of SK1-EC30 is about 2 times lower than that of SK2-EC30.

Generally, as eccentricity distances increase, the ultimate load of the specimen tends to be decreased in all cases. The numerical model reveals the ultimate load is significantly influenced by the distance of eccentricity. Relative to the models, there is a gradual reduction in load discrepancies within the SK2 model, whereas the ultimate load of the SK1 model changes quite quickly, potentially attributable to variations in the number of shear keys. The two shear keys clearly increased the others in shear resistance and deformation. As the shear key number was increased from one to two, the elastic shear stiffness, and ultimate and residual shear forces of SK2 rose. Compared with other circumstances, the elastic shear stiffness of the two shear keys increased than the other cases, while the residual load rose by two to three times. In addition, the final load was three to four times greater than in the other cases.

By considering the eccentricity effects, numerical models under actual states were proposed for predicting the ultimate load of structures. In the future, the findings of this study can be utilized for optimizing the shape of UHPC rib design in residential buildings by using these parameters within a defined range.

Table 9
Modeling recommendations.

Component	Constitutive model	Parameter	Value
UHPC	*MAT072R3	Table 4	
Normal concrete	*MAT084/085	RATE 0	Default
Reinforcing steel	*MAT003	Hardening parameter	0.2
Loading part	*MAT_RIGID_(020)		
Contact	_SURFACE_TO_SURFACE	Penalty stiffness	1
Bar-concrete interface	*CONSTRAINED_LAGRANGE_IN_SOLID	Perfect bond	

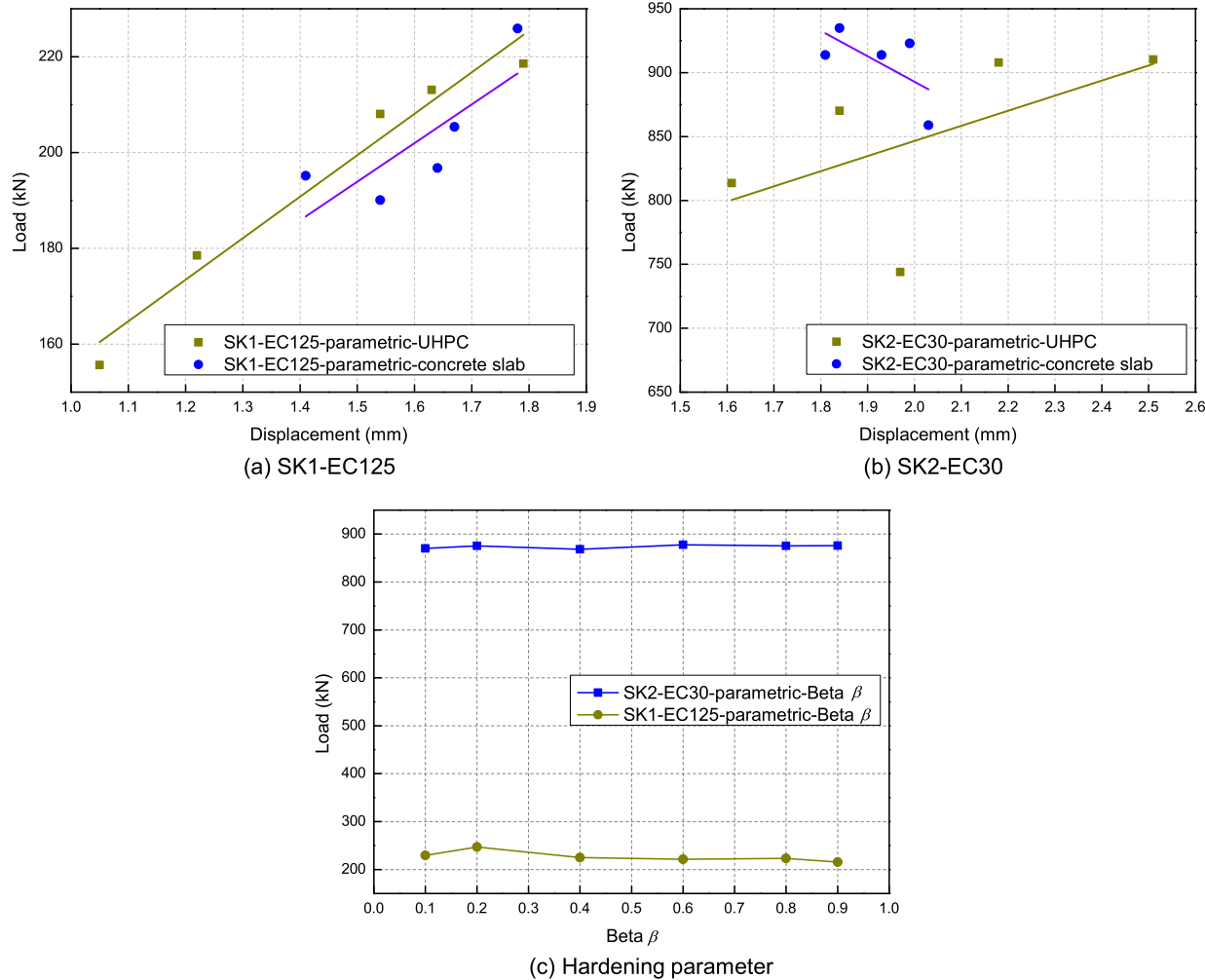


Fig. 23. Effect of concrete strength and hardening parameter on the peak lateral force.

7. Conclusion

Novel connections have been developed for the UHPC rib and cladding wall in buildings to improve structural performance compared to the conventional solution. A total of five specimens were built and tested under static loading conditions to investigate the behavior of this connection. The behavior of the reinforced concrete structures were simulated by models in LS-DYNA. Five models were built to compare with the experimental results, using both the KCC and Winfrith in one model. The results obtained from the simulation demonstrated that the model could acceptably estimate crack failure and the load-displacement curve. In addition, parametric studies of the concrete strength, and eccentricity distances were conducted to find the failure mode and the peak load with one and two shear keys for UHPC rib cases. The following conclusions can be drawn from the results of the experiment and the numerical model:

- The shear capacity of the UHPC rib connection cladding wall was influenced significantly by the number of shear keys and loading positions. For the specimen with 2 shear keys, which enhanced the load capacity about 3 to 4 times in comparison with 1 shear key, without shear key specimens. In addition, the ultimate load of the specimens is generally decreased with an increase in eccentricity distance across all cases.
- Almost all of the failure modes observed in the experiment occurred on the cladding wall, except the RC-EC100 specimen. Due to the concrete's monolithic placement by the in situ cast solution, there was an increase in load capacity compared to SK0-EC100. In contrast, the concrete strength of the SK0-EC100 specimen was different using wall and rib concrete, leading to crack failure occurring in the connection position.
- For the RC-EC100 specimen, diagonal cracks were observed in the rib. There was an increase in load capacity compared with SK0-

EC100 because the concrete was placed monolithically by the in situ cast solution. In contrast, the concrete strength of the SK0-EC100 specimen was different using wall and rib concretes lead to crack failure occurred in the connection position.

- The models were verified by comparison with the experimental results from five specimens. The curves of the rib were recorded with peak load differences of about 5.85%, to compare with the experiment. The shapes of the load against displacement curve were in agreement with the measured responses.
- The parametric study used UHPC compressive strengths ranging from 25 MPa to 50 MPa for the wall and 150 MPa to 200 MPa for the UHPC rib. This allowed for the prediction of the peak load and crack failure inside and outside of the UHPC rib and cladding wall. However, there were small differences in these results, about 3.62%, 7.08%, and 0.73%, 3.46% for the SK1-EC125 and SK2-EC30 cases, respectively. In addition, the UHPC rib shape was unchanged during the simulation. Therefore, the concrete strength of the UHPC rib can be reduced while still maintaining safety and saving on building costs.
- This paper provided parameters and results that were used to examine the accuracy of the modeling methods for both reinforced concrete and rebars. These results and recommendations regarding the constitutive model, the bar-concrete interface, as well as the value of conventional concrete and reinforcing steel may be of value to other researchers using the LS-DYNA software. It is clear that the load capacity was significantly influenced by a variety of factors, including the number, shape, cross-sectional area of the shear keys, and strength of the concrete and rebar. The results of the simulation analysis and testing showed that this is an appropriate structure for future thermal bridges, even though the dimensions, shape, and material properties of the UHPC ribs can be changed.

However, in this work, one limitation of the study is the relatively small number of specimens tested. This limited number of specimens may potentially restrict the generalizability to different structure specifications. Employing a larger of specimens would facilitate a more robust statistical analysis, ultimately enhancing the reliability and generalizability of the conclusions drawn from this research. In future studies, the structural performance of these solutions will be conducted simultaneously under diverse situational contexts.

CRediT authorship contribution statement

Nguyen Huu Cuong: Writing – review & editing, Writing – original draft, Validation, Software, Methodology, Investigation, Conceptualization. **Hyoseo An:** Writing – review & editing, Investigation. **Tran-Van Han:** Validation, Software, Methodology, Data curation. **Sanghee An:** Writing – review & editing, Software. **Jiuk Shin:** Writing – review & editing, Formal analysis. **Kihak Lee:** Writing – review & editing, Supervision, Resources, Project administration, Formal analysis.

Declaration of competing interest

The authors declare that they have no known competing financial interests or personal relationships that could have appeared to influence the work reported in this paper.

Data availability

The authors do not have permission to share data.

Acknowledgements

This research was supported by Basic Science Research Program through the National Research Foundation of Korea (NRF) funded

by the Ministry of Education (RS-2023-00271991) and supported by JeongYang SG Co., Ltd.

Appendix A. Results of parametric studies obtained from LS-DYNA

See Tables A.10–A.12.

Table A.10
Abbreviations used.

Abbreviation	Definition
SK0-EC100	PC2-SK0-Ecc0
SK1-EC100	PC2-SK1-Ecc0
SK1-EC125	PC2-SK1-Ecc50
SK2-EC30	PC2-SK2-Ecc0
RC-EC100	RC-slab-rib

Table A.11
Results of parametric studies.

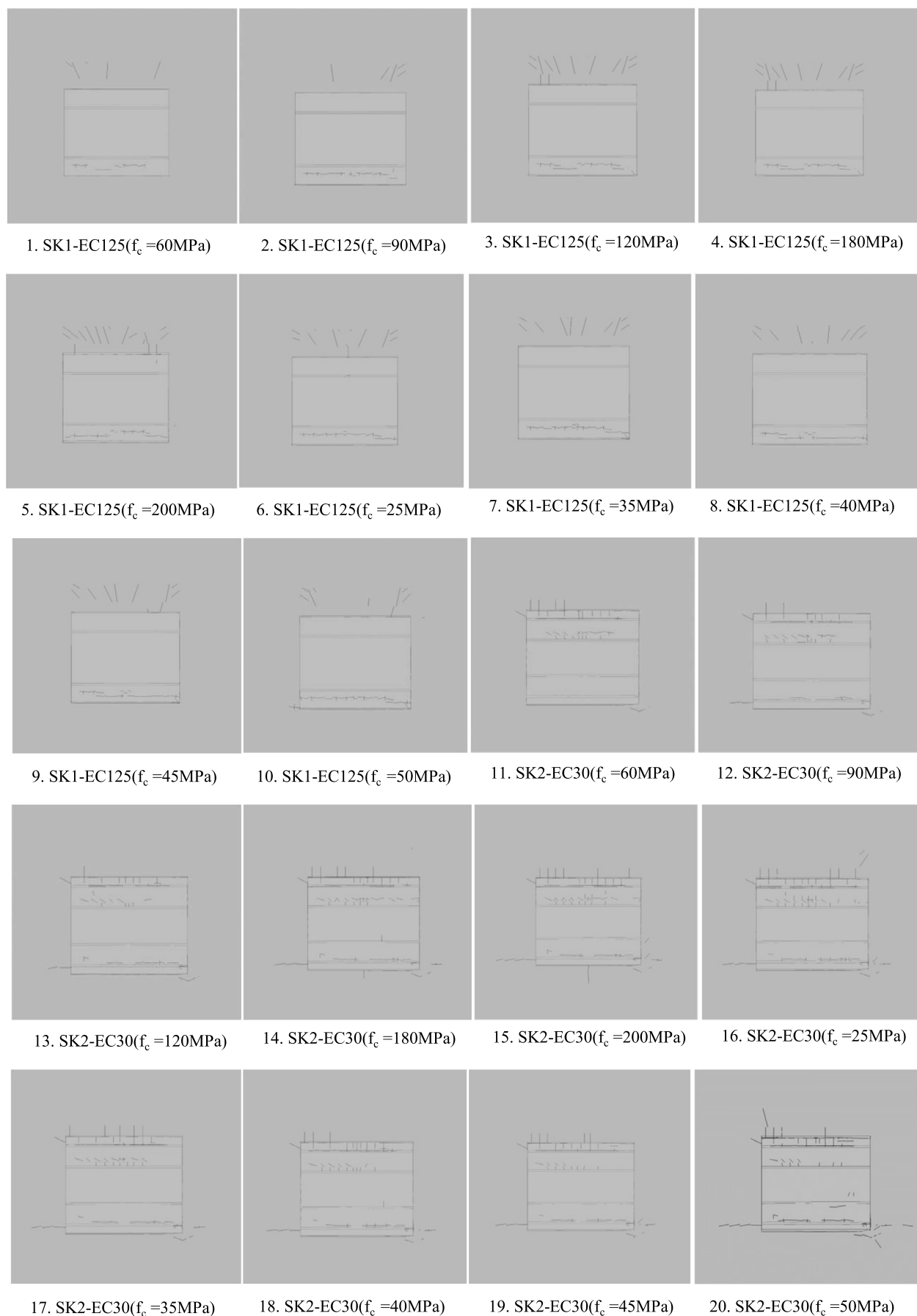
No.	Model	Strength concrete		Peak load	Displacement	Shear key
		UHPC rib	Wall			
1	SK1-EC125	60	36.1	155.64	1.05	1
2		90	36.1	178.52	1.22	1
3		120	36.1	208.03	1.54	1
4		180	36.1	213.05	1.63	1
5		200	36.1	218.54	1.79	1
6		152.5	25.0	225.85	1.78	1
7		152.5	35.0	205.32	1.67	1
8		152.5	40.0	196.76	1.64	1
9		152.5	45.0	195.13	1.41	1
10		152.5	50.0	190.06	1.54	1
11	SK2-EC30	60	36.1	743.94	1.97	2
12		90	36.1	813.56	1.61	2
13		120	36.1	870.11	1.84	2
14		180	36.1	907.87	2.18	2
15		200	36.1	910.23	2.51	2
16		152.5	25.0	858.93	2.03	2
17		152.5	35.0	922.89	1.99	2
18		152.5	40.0	913.71	1.93	2
19		152.5	45.0	913.84	1.81	2
20		152.5	50.0	934.94	1.84	2

Table A.12
Results of parametric studies.

No.	Model	Strength concrete		Peak load	Parameter β	Shear key
		UHPC rib	Wall			
21	SK1-EC125	152.5	36.1	229.35	0.1	1
22		152.5	36.1	247.01	0.2	1
23		152.5	36.1	224.79	0.4	1
24		152.5	36.1	221.21	0.6	1
25		152.5	36.1	223.09	0.8	1
26		152.5	36.1	215.66	0.9	1
27		152.5	36.1	870.24	0.1	2
28		152.5	36.1	875.38	0.2	2
29		152.5	36.1	868.16	0.4	2
30		152.5	36.1	877.53	0.6	2
31	SK2-EC30	152.5	36.1	875.23	0.8	2
32		152.5	36.1	875.8	0.9	2

Appendix B. Crack and failure of numerical models

See Fig. B.24.

**Fig. B.24.** Crack and failure of numerical models.

References

- [1] H. Ge, V.R. McClung, S. Zhang, Impact of balcony thermal bridges on the overall thermal performance of multi-unit residential buildings: a case study, *Energy Build.* 60 (2013) 163–173, <https://doi.org/10.1016/J.ENBUILD.2013.01.004>.
- [2] T.G. Theodosiou, A.M. Papadopoulos, The impact of thermal bridges on the energy demand of buildings with double brick wall constructions, *Energy Build.* 40 (2008) 2083–2089, <https://doi.org/10.1016/J.ENBUILD.2008.06.006>.
- [3] T. Keller, F. Riebel, A. Zhou, Multifunctional all-GFRP joint for concrete slab structures, *Constr. Build. Mater.* 21 (2007) 1206–1217, <https://doi.org/10.1016/J.CONBUILDMAT.2006.06.003>.
- [4] F. Riebel, T. Keller, Long-term compression performance of a pultruded GFRP element exposed to concrete pore water solution, *J. Compos. Constr.* 11 (2007) 437–447, [https://doi.org/10.1061/\(ASCE\)1090-0268\(2007\)11:4\(437\)](https://doi.org/10.1061/(ASCE)1090-0268(2007)11:4(437)).
- [5] F. Riebel, T. Keller, Structural behavior of multifunctional GFRP joints for concrete structures, *Constr. Build. Mater.* 23 (2009) 1620–1627, <https://doi.org/10.1016/J.CONBUILDMAT.2008.05.013>.
- [6] N.H. Cuong, H. An, H.V. Tran, S. An, K. Lee, Structural test and analyses of uhpc horizontal connection with shear keys for slab-external pc wall, *Constr. Build. Mater.* 419 (2024) 135410, <https://doi.org/10.1016/j.conbuildmat.2024.135410>.
- [7] M.A. Bajaber, I.Y. Hakeem, UHPC evolution, development, and utilization in construction: a review, *J. Mater. Res. Technol.* 10 (2021) 1058–1074, <https://doi.org/10.1016/J.JMRT.2020.12.051>.
- [8] M. Ramadan, D.M. Ors, A.M. Farghal, A. Afifi, A.H. Zaher, A.M. Ebid, Punching shear behavior of hsc and uhpc post tensioned flat slabs – an experimental study, *Results Eng.* 17 (2023) 100882, <https://doi.org/10.1016/j.rineng.2023.100882>.
- [9] J. Xue, B. Briseghella, F. Huang, C. Nuti, H. Tabatabai, B. Chen, Review of ultra-high performance concrete and its application in bridge engineering, *Constr. Build. Mater.* 260 (2020) 119844, <https://doi.org/10.1016/J.CONBUILDMAT.2020.119844>.
- [10] N.H. Cuong, L. Gayoon, H. An, S. An, S.W. Han, K. Lee, Experimental evaluation of a vertical heat bridge insulation system for the structural performance of multi-residential buildings, *Structures* 58 (2023) 105686, <https://doi.org/10.1016/j.istruc.2023.105686>.
- [11] M. Schmidt, E. Fehling, *Ultra-High-Performance Concrete: Research, Development and Application in Europe*, 2005.
- [12] Y. Huang, J. Wang, Q. Wei, H. Shang, X. Liu, Creep behaviour of ultra-high-performance concrete (uhpc): review, *J. Build. Eng.* 69 (2023) 106187, <https://doi.org/10.1016/j.jobe.2023.106187>.
- [13] S. Abdal, W. Mansour, I. Agwa, M. Nasr, A. Abadel, Y. Onuralp Özklıç, M.H. Akeed, Application of ultra-high-performance concrete in bridge engineering: current status, limitations, challenges, and future prospects, *Buildings* 13 (2023), <https://doi.org/10.3390/buildings13010185>.
- [14] V. Kodur, S. Banerji, R. Solmimirzaei, Effect of temperature on thermal properties of ultrahigh-performance concrete, *J. Mater. Civ. Eng.* 32 (2020) 04020210, [https://doi.org/10.1061/\(ASCE\)MT.1943-5533.0003286](https://doi.org/10.1061/(ASCE)MT.1943-5533.0003286).
- [15] M. Abid, X. Hou, W. Zheng, R.R. Hussain, High temperature and residual properties of reactive powder concrete – a review, *Constr. Build. Mater.* 147 (2017) 339–351, <https://doi.org/10.1016/J.CONBUILDMAT.2017.04.083>.
- [16] S. Aghasizadeh, B.M. Kari, R. Fayaz, Thermal performance of balcony thermal bridge solutions in reinforced concrete and steel frame structures, *J. Build. Eng.* 48 (2022) 103984, <https://doi.org/10.1016/J.JOBE.2021.103984>.
- [17] T. Wang, O. Hopperstad, P. Larsen, O.-G. Lademo, Evaluation of a finite element modelling approach for welded aluminium structures, *Comput. Struct.* 84 (2006) 2016–2032, <https://doi.org/10.1016/j.compstruc.2006.08.011>.
- [18] W. Feng, B. Chen, F. Yang, F. Liu, L. Li, L. Jing, H. Li, Numerical study on blast responses of rubberized concrete slabs using the karagozian and case concrete model, *J. Build. Eng.* 33 (2021) 101610, <https://doi.org/10.1016/j.jobe.2020.101610>.
- [19] H. Yin, K. Shirai, W. Teo, Numerical model for predicting the structural response of composite UHPC-concrete members considering the bond strength at the interface, *Compos. Struct.* 215 (2019) 185–197, <https://doi.org/10.1016/J.COMPSTRUCT.2019.02.040>.
- [20] A. Al Ali, E. Arhore, H. Ghasemnejad, M. Yasaee, Experimental and numerical investigation of multi-layered honeycomb sandwich composites for impact mechanics applications, *Results Eng.* 21 (2024) 101817, <https://doi.org/10.1016/j.rineng.2024.101817>.
- [21] S. Azad, S.R. Mirghaderi, S. Epakachi, Numerical investigation of steel and composite beam-to-encased composite column connection via a through-plate, *Structures* 31 (2021) 14–28, <https://doi.org/10.1016/J.ISTRUC.2021.01.040>.
- [22] M. Asgarpoor, A. Gharavi, S. Epakachi, Investigation of various concrete materials to simulate seismic response of RC structures, *Structures* 29 (2021) 1322–1351, <https://doi.org/10.1016/J.ISTRUC.2020.11.042>.
- [23] J. Duic, S. Kenno, S. Das, Performance of concrete beams reinforced with basalt fibre composite rebar, *Constr. Build. Mater.* 176 (2018) 470–481, <https://doi.org/10.1016/J.CONBUILDMAT.2018.04.208>.
- [24] I. Zafar, T. Sugiyama, The influence of bending crack on rebar corrosion in fly ash concrete subjected to different exposure conditions under static loading, *Constr. Build. Mater.* 160 (2018) 293–307, <https://doi.org/10.1016/J.CONBUILDMAT.2017.11.070>.
- [25] I.H. Yang, C. Joh, B.S. Kim, Structural behavior of ultra high performance concrete beams subjected to bending, *Eng. Struct.* 32 (2010) 3478–3487, <https://doi.org/10.1016/J.ENGSTRUCT.2010.07.017>.
- [26] S.M. Ayatollahi Moosavi, R. Tabatabaei Mirhoseini, M. Kebriaie, Investigation of seismic behavior of the reinforced concrete wall-frame system on a flexible bed, *Results Eng.* 15 (2022) 100581, <https://doi.org/10.1016/j.rineng.2022.100581>.
- [27] A. C1856/C1856M-17, *Standard Practice for Fabricating and Testing Specimens of Ultra-High Performance Concrete*, ASTM International, West Conshohocken, PA, 2017.
- [28] B.A. Graybeal, Compression testing of ultra-high-performance concrete, *Adv. Civ. Eng. Mater.* 4 (2015) 102–112, <https://doi.org/10.1520/ACEM20140027>.
- [29] C. ASTM, 39/C 39M: The American Society for Testing Materials, *Standard Test Method for Compressive Strength of Cylindrical Concrete Specimens*, West Conshohocken (PA), USA, 2001.
- [30] M. Hu, Q. Han, S. Wu, X. Du, Shear capacity of precast concrete shear keys with ultrahigh-performance concrete for connections, *J. Bridge Eng.* 26 (2021) 04201036, <https://doi.org/10.1016/J.STRUCTURE.2021.04201036>.
- [31] R. Pan, L. Cheng, W. He, X. Zhou, X. Shen, Direct shear performance of UHPC multi-keyed epoxy joint, *Structures* 44 (2022) 1898–1909, <https://doi.org/10.1016/J.ISTRUC.2022.08.094>.
- [32] B.A. Gopal, F. Hejazi, M. Hafezolghorani, V. Yen Lei, Numerical analysis and experimental testing of ultra-high performance fibre reinforced concrete keyed dry and epoxy joints in precast segmental bridge girders, *Int. J. Adv. Struct. Eng.* 11 (2019) 463–472, <https://doi.org/10.1007/S40091-019-00246-6/FIGURES/7>.
- [33] Shin Jaewoo, *Ultra-high performance concrete (UHPC) precast segmental bridges: flexural behaviour and joint design*, Hamburg (2016).
- [34] T. Shi, X. Zhang, H. Hao, G. Xie, Experimental and numerical studies of the shear resistance capacities of interlocking blocks, *J. Build. Eng.* 44 (2021) 103230, <https://doi.org/10.1016/J.JOBEL.2021.103230>.
- [35] G. Rombach, A. Specker, *Design of Joints in Segmental Hollow Box Girder Bridges*, 2002.
- [36] JSCE, *Standard Specifications for Concrete Structures*, 2007, Design Japan Society of Civil Engineers, JSCE Guidelines for Concrete, 2007.
- [37] M.K. Kim, D.J. Kim, Y.K. An, Electro-mechanical self-sensing response of ultra-high-performance fiber-reinforced concrete in tension, *Composites, Part B, Eng.* 134 (2018) 254–264, <https://doi.org/10.1016/J.COMPOSITESB.2017.09.061>.
- [38] M.A. Issa, H.A. Abdalla, Structural behavior of single key joints in precast concrete segmental bridges, *J. Bridge Eng.* 12 (2007) 315–324, [https://doi.org/10.1016/J.JOBEL.2007.12.3\(315\)](https://doi.org/10.1016/J.JOBEL.2007.12.3(315)).
- [39] K. Yoshio, J.J. Connor, T.C. Triantafillou, C.K. Leung, Fracture mechanics approach for failure of concrete shear key. I: theory, *J. Eng. Mech.* 119 (1993) 681–700, [https://doi.org/10.1016/0733-9399\(1993\)119:4\(681\).1](https://doi.org/10.1016/0733-9399(1993)119:4(681).1).
- [40] D.K. Thai, S.E. Kim, Failure analysis of uhpfrc panels subjected to aircraft engine model impact, *Eng. Fail. Anal.* 57 (2015) 88–104, <https://doi.org/10.1016/j.engfailanal.2015.07.005>.
- [41] H. Selim Şengel, H. Erol, T. Yılmaz, Ö. Anıl, H. Can Gürdal, A. Muhammed Uludoğan, Low-velocity impact behavior of two-way RC slab strengthening with carbon TRM strips, *Structures* 44 (2022) 1695–1714, <https://doi.org/10.1016/J.ISTRUC.2022.08.108>.
- [42] S. Şengel, H. Erol, T. Yılmaz, Ö. Anıl, Investigation of the effects of impactor geometry on impact behavior of reinforced concrete slabs, *Eng. Struct.* 263 (2022) 114429, <https://doi.org/10.1016/J.ENGSTRUCT.2022.114429>.
- [43] M.Z. Zhao, D.E. Lehman, C.W. Roeder, Modeling recommendations for RC and CFST sections in LS-Dyna including bond slip, *Eng. Struct.* 229 (2021) 111612, <https://doi.org/10.1016/J.ENGSTRUCT.2020.111612>.
- [44] L. Ren, X. Yu, Y. He, K. Wang, H. Yao, Numerical investigation of lateral inertia effect in dynamic impact testing of UHPC using a Split-Hopkinson pressure bar, *Constr. Build. Mater.* 246 (2020) 118483, <https://doi.org/10.1016/J.CONBUILDMAT.2020.118483>.
- [45] L.J. Malvar, J.E. Crawford, J.W. Wesevich, D. Simons, A plasticity concrete material model for DYNA3D, *Int. J. Impact Eng.* 19 (1997) 847–873, [https://doi.org/10.1016/S0734-743X\(97\)00023-7](https://doi.org/10.1016/S0734-743X(97)00023-7).
- [46] Y. Wu, J.E. Crawford, Numerical modeling of concrete using a partially associative plasticity model, *J. Eng. Mech.* (2015) 04015051, <https://doi.org/10.1016/ASCE.EM.1943-7889.0000952>.
- [47] Material Properties, *CEB-FIP Model Code 1990, 1993*, pp. 33–81.
- [48] F.H. Wittmann, K. Rokugo, E. Brihwiler, H. Mihashi, P. Simonin, Fracture energy and strain softening of concrete as determined by means of compact tension specimens, *Mater. Struct.* 21 (1) (1988) 21–32, <https://doi.org/10.1007/BF02472525>.
- [49] Download/Order LSTC Product Manuals | Livermore Software, Software Technology Corp., 2022.
- [50] G. Tunc, M.M. Othman, H.C. Mertol, Finite element analysis of frames with reinforced concrete encased steel composite columns, *Buildings* 2022 12 (2022) 375, <https://doi.org/10.3390/BUILDINGS12030375>.
- [51] S. Xu, B. Chen, Q. Li, F. Zhou, X. Yin, X. Jiang, P. Wu, Experimental and numerical investigations on ultra-high toughness cementitious composite slabs subjected to close-in blast loadings, *Cem. Concr. Compos.* 126 (2022) 104339, <https://doi.org/10.1016/J.CEMCONCOMP.2021.104339>.